Rational design of gelatin/nanohydroxyapatite cryogel scaffolds for bone regeneration by introducing chemical and physical cues to enhance osteogenesis of bone marrow mesenchymal stem cells

K.T. Shalumon[a,1], Han-Tsung Liao[b,1], Chang-Yi Kuo[a], Chak-Bor Wong[c], Chien-Ju Li[a], Mini P.A.[d], Jyh-Ping Chen[a,b,e,f,*]

[a] Department of Chemical and Materials Engineering, Chang Gung University, Kwei-San, Taoyuan 33302, Taiwan, ROC
[b] Department of Plastic and Reconstructive Surgery and Craniofacial Research Center, Chang Gung Memorial Hospital, Chang Gung University School of Medicine, Kwei-San, Taoyuan 33305, Taiwan, ROC
[c] Department of Orthopaedic Surgery, Chang Gung Memorial Hospital, Keelung 20401, Taiwan, ROC
[d] Department of Physics, St. Michael's College, Cherthala Alappuzha, Kerala 688539, India
[e] Research Center for Food and Cosmetic Safety, Research Center for Chinese Herbal Medicine, College of Human Ecology, Chang Gung University of Science and Technology, Taoyuan 33302, Taiwan, ROC
[f] Department of Materials Engineering, Ming Chi University of Technology, Tai-Shan, New Taipei City 24301, Taiwan, ROC

ARTICLE INFO

ABSTRACT

Identification of key components in the chemical and physical milieu for directing osteogenesis is a requirement in the investigation of tissue engineering scaffolds for advancement of bone regeneration. In this study, we engineered different gelatin-based cryogels and studied the effect of nanohydroxyapatite (nHAP) and cross-linking agents on scaffold properties and its osteogenic response towards bone marrow stem cells (BMSCs). The cryogels examined are 5% gelatin and 5% gelatin/2.5% nHAP, crosslinked either with 1-ethyl-3-(3-dimethyla-minopropyl)-carbodiimide (EDC) or glutaraldehyde (GA). We confirmed that nHAP or the crosslinking agent has no effects on scaffold pore size and porosity. Nonetheless, incorporation of nHAP increased mechanical strength, swelling ratio and degree of crosslinking, but decreased degradation rate. Cryogels crosslinked with EDC showed faster degradation and promoted osteogenic differentiation of BMSCs while those prepared from GA crosslinking promoted proliferation of BMSCs. Furthermore, osteogenic differentiation was always enhanced in the presence of nHAP irrespective of the culture medium (normal or osteogenic) used but osteogenic medium always provide a higher extent of osteogenic differentiation. Employing gelatin/nHAP cryogel crosslinked by EDC in a bior-eactor for dynamic culture of BMSCs, cyclic compressive mechanical simulation was found to be beneficial for both cell proliferation and osteogenic differentiation. However, the optimum conditions for osteogenic differentiation and cell proliferation were found at 30% and 60% strain, respectively. We thus demonstrated that osteogenic differentiation of BMSCs could be tuned by taking advantages of chemical cues generated from scaffold chemistry or physical cues generated from dynamic cell culture in vitro. Furthermore, by combining the best cryogel preparation and in vitro cell culture condition for osteogenesis, we successfully employed in vitro cultured cryogel/BMSCs constructs for repair of rabbit critical-sized cranial bone defects.

1. Introduction

Gelatin is a heterogeneous mixture of water-soluble proteins produced by partial hydrolysis of collagen, which in many aspects is closely similar in chemical composition to collagen. In tissue engineering, scaffolds are designed to function as a temporary and artificial extra-cellular matrix (ECM) to support cell attachment and guide three-dimensional (3D) tissue formation in vivo [1–3]. Being attractive in affordability, biodegradability and good biocompatibility, gelatin has been selected as a scaffolding material over the years to bypass the concerns of immunogenicity and pathogen transmission associated with collagen while still could mimic the biological ECM [4–7]. Bone tissue is a combination of ECM and cells with the composite ECM being mainly composed of nanofibrous collagen type I (COL I) and partially

---

carbonated hydroxyapatite (HAP) [8]. Though it is one of the prime components of ECM, using HAP alone scaffold fabrication is limited due to the processing difficulty stemming from the brittle nature of HAP. In this aspect, the combination of HAP and gelatin in a single scaffold would therefore provide favorable properties from both HAP and gelatin [9].

Nanohydroxyapatite (nHAP) is similar to native HAP in bone with well-known biocompatibility and osteoconductive properties [10]. Many nHAP-based composite scaffolds fabricated from natural or synthetic polymers have been explored as bone graft substitutes for bone regeneration with improved bone properties [11]. nHAP can enhance cell-material interactions and the bioactivity of HAP-based synthetic grafts compared to larger size HAP particles [12]. Being a resource of free calcium, nHAP was reported to possess higher osteoconductivity than micro-sized HAP and to be suitable for the osteogenic process [13]. Additionally, nHAP has a positive effect on protein adhesion, cell adhesion, proliferation and osteointegration [14]. A 3D gelatin/chitosan scaffold embedded with nHAP with well-defined macropores was reported to mimic bone ECM and provide an ideal environment for bone regeneration from human induced pluripotent stem cells [15].

Cryogelation is a simple and effective method for producing macroporous scaffolds having controlled pore size [16]. This method allows effective control over the pore size using ice crystals as templates for producing macroporous scaffold structure. During the cryogelation process, a polymer solution was mixed with a crosslinking agent, which was allowed to undergo freezing, chemical crosslinking and subsequent thawing steps [17]. As the matrices are allowed to crosslink at sub-zero temperatures, the ice crystals formed within the scaffold act as porogen and result in interconnected pores within the gelled matrix after thawing. Considering various properties of cryogels such as their interconnected pores, elasticity, mechanical stability, reversibility and swelling ability, it would be suitable for tissue regeneration [18,19]. Nonetheless, stability of the cryogel scaffold still depends on the extent of crosslinking, nature of the crosslinking agent, and concentrations of the polymer solutions.

One of the challenges in the field of bone tissue engineering is the construction of comparable *in vitro* environments to native tissue for growing cells or tissues [20]. Essential to this paradigm are stimulating factors that promote the osteoinductive capacity of the scaffold, which include chemical and physical (electromagnetic and mechanical) stimuli [21]. Effects of chemical stimuli on bone formation using cryogel scaffolds have been studied before but not in the case of physical stimuli [22]. Using electromagnetic stimulation on mesenchymal stromal cells seeded in gelatin cryogels, Saino et al. reported enhanced cell proliferation and osteogenic differentiation and elevated production of bone marker proteins COL I, osteocalcin (OCN) and osteopontin (OPN) [23]. Gelatin cryogel seeded with human osteosarcoma cells in a bioreactor with electromagnetic stimulation resulted in more bone matrix production [24]. Studies using ultrasound on gelatin cryogels seeded with human osteosarcoma cells [25] and electric stimulation to composite cryogels seeded with C2C12 myoblasts also confirmed faster bone regeneration [26]. As one form of physical stimuli, mechanical stimulation has been used as a tool for promoting the development of a number of tissue types *in vitro*, including bone [27], cartilage [28], skeletal muscle [29], ligament and cardiac muscle [30].

The main goal of current study is to design 3D gelatin/nanohydroxyapatite (nHAP) cryogels and to test the hypothesis that mechanical stimulation in a bioreactor could promote osteogenic differentiation of bone marrow-derived stem cells (BMSCs) *in vitro*. For this purpose, factors pertaining to rational design of the cryogel scaffolds were studied, starting from a comprehensive evaluation of material characteristics to *in vivo* bone regeneration. The influence of nHAP and crosslinking agents, including glutaraldehyde (GA) and 1-ethyl-3-(3-dimethylaminopropyl)-carbodiimide (EDC), was verified through physico-chemical characterizations and cellular response of bone marrow stem cells (BMSCs) was evaluated *in vitro*. Although the combination of

nHAP and gelatin in a bone tissue engineering scaffold is well established, gelatin/nHAP cryogel was selected here due to its unique elastic property to provide facile dynamic mechanical compression towards differentiation of BMSCs and meaningful comparison of the regeneration potential in a stimuli-responsive mode. Using such *in-situ* stimulated *in vitro*-cultured scaffolds, the optimized cryogel/cell construct intended for bone tissue engineering was ultimately tested *in vivo* in a critical-sized rabbit cranial bone defect model.

2. Materials and methods

2.1. Materials

Glutaraldehyde (GA), 2-morpholinoethane sulfonic acid (MES), gelatin (type A from porcine skin, 300 bloom) and 2,4,6-trinitrobenzene sulfonic acid (TNBS) were purchased from Sigma-Aldrich. Fetal bovine serum (FBS) was obtained from HyClone. N-Hydroxysuccinimide (NHS) and 1-ethyl-3-(3-dimethylaminopropyl) carbodiimide (EDC) were procured from Acros. 6-Diamidino-2-phenylindole dihydrochloride (DAPI) and rhodamine phalloidin (phalloidin conjugated with tetra-methylrhodamine isothiocyanate) were purchased from Life Technologies. Dulbecco's Modified Eagle Medium (DMEM) was obtained from Gibco.

2.2. Synthesis of nHAP

The nHAP was synthesized through chemical precipitation as reported in our previous study [31]. Briefly, 0.86 g of $CaHPO_4.2H_2O$ and 0.335 g of $CaCO_3$ were gently mixed in a 2.5 M NaOH solution at 75 °C and further reacted for 1 h. After terminating the reaction in an ice bath, the solution was centrifuged and washed multiple times with double distilled water. The obtained slurry was dried at 70 °C for 24 h to obtain nHAP.

2.3. Preparation of gelatin and gelatin/nHAP composite cryogels

A gelatin solution with an initial concentration of 10%(w/w) was prepared in distilled deionized (DDI) water in a 70 °C water bath (solution A1). The crosslinking agent GA was prepared in DDI water with an initial concentration of 0.02 M (solution A2). Another gelatin solution with 10%(w/w) concentration was prepared similarly by dissolving gelatin flakes in MES buffer (pH = 6.5) (solution B1). The crosslinking agent EDC was prepared in MES buffer (pH = 6.5) at 0.02 M (solution B2). A solution was prepared at 70 °C by mixing equal volume of A1 and A2 or B1 and B2 solutions to crosslink 5% gelatin with 0.01 M GA in DDI water or with 0.01 M EDC in pH 6.5 MES buffer. In both cases, the pre-mixed solution was placed in an end-capped 3 ml plastic syringe (Terumo, inner diameter = 8.5 mm), followed by mixing with a home-made vibration-free overhead spindle stirrer. Stirring was maintained in such a way to avoid air bubble formation, which could lead to uneven pore formation in the cryogel. After closing the top end of the syringe mold with Parafilm Wrap (Cole-Parmer), the mold was immersed in a 95% ethanol bath at − 16 °C in a freezer and crosslinked for 16 h to complete the cryogelation process. After completion of the reaction, the syringe mold was taken out of the bath and the gel was allowed to recede through the bottom cap after thawing. The gel was cut into cylindrical-shaped discs (8 mm diameter × 2 mm thickness). The unreacted aldehyde groups in GA-crosslinked cryogels were blocked after immersing the disc-shaped scaffolds with 0.01 M glycine in phosphate buffered saline (PBS) for 2 h. The prepared cryogels were washed with copious DDI water at 70 °C for 4 h to obtain macroporous cryogel scaffolds [32]. The preparation of gelatin/nHAP composite cryogels followed the same procedure but using solution A1 prepared in DDI water containing 10% gelatin/5% nHAP and solution B1 prepared in pH 6.5 MES buffer containing 10% gelatin/5% nHAP to obtain 5% gelatin/2.5% nHAP composite cryogels. Gelatin (gelatin/nHAP) cryogel

scaffolds synthesized using EDC and GA will be referred to as G-EDC (Gn-EDC) and G-GA (Gn-GA), respectively.

2.4. Characterization of cryogels

The morphology of cryogel was characterized using scanning electron microscopy (SEM) (Hitachi S-3000N) whereas the elemental composition was estimated through energy dispersive X-ray spectroscopy (EDS) (Horiba EX-250). Chemical compositions were identified through Fourier-transform infrared spectroscopy (FTIR) (Horiba FT-730) from 400 to 4000 cm^{-1} with $2\,cm^{-1}\,s^{-1}$ resolutions. The cryo-frozen samples were ground to fine powder in a mortar and mixed with dry KBr at 1:8 mass to make 1-cm diameter disc-shaped samples for FTIR analysis. X-ray diffraction (XRD) patterns of cryogels were recorded using a Siemens D5005 X-ray diffractometer having a CuKa source, a quartz monochromator and a goniometric plate at $2°\,min^{-1}$ from 10 to 60°. The spectra were recorded as intensity *vs* 2θ value. Pore size was determined for a cryo-sectioned sample of 0.5 mm thickness by capillary flow porosimetry (PMI CFP-1100-AI, Porous Materials Inc.) with nitrogen gas from 0 to 5 psi and using ethanol as the wetting agent [33]. Porosity of the scaffold was determined using the ethanol displacement method [18]. The crosslinking density was evaluated by 2,4,6-trinitrobenzenesulfonic acid (TNBSA) assay after reacting free amino groups in a cryogel with TNBSA and a standard curve generated from glucosamine [34]. The degree of cross-linking (DC) was calculated from the amount of free amino groups in the sample after normalization with the mass of the sample,

$$\text{Degree of cross linking } (\%) = \left[1 - \frac{\left(\frac{free\ amino\ groups}{mass} \right)_c}{\left(\frac{free\ amino\ groups}{mass} \right)_{nc}} \right] \times 100 \tag{1}$$

where *c* and *nc* represent crosslinked and non-crosslinked samples, respectively.

The swelling ratios were evaluated through gravimetric procedure [18]. A dried cryogel sample was immersed in DDI water at room temperature for 24 h and the swelling ratio was calculated from the weight of the swollen sample after removing excess water from the sample,

$$\text{Swelling ratio} = (W_e - W_1)/W_1 \tag{2}$$

where W_e is the equilibrium mass of the wet cryogel and W_1 is the mass of dry cryogel.

The degradation studies were performed in PBS or 0.01 mg/ml collagenase in PBS by calculating the degree of degradation.

$$\text{Degree of degradation } (\%) = \frac{(W_1 - W_2)}{W_1} \times 100 \tag{3}$$

where W_1 is the mass of initial dry cryogel and W_2 is the mass of dry cryogel after immersing in the solution for different time intervals.

The dynamic and quasi-static mechanical behavior of the cryogel scaffolds were evaluated through compression testing on wet cryogel samples (soaking in PBS for 24 h) using an ElectroForce® 5200 BioDynamic™ Test Instrument (Bose). A uniaxial stress was generated from a 250 N load cell with a cross-head speed of 0.02 mm/s to obtain the stress (σ) *vs* strain (ε) curve. The point at which failure of the cryogel occurred determined the ultimate compressive strain and ultimate stress. A non-linear equation was used to curve-fit the stress–strain data up to failure [35].

$$\sigma = Ae^{(B\varepsilon - 1)} \tag{4}$$

with A and B being fitted constants. The elastic modulus at 30% strain was calculated using the non-linear elastic model. The toughness (compressive strain energy to failure) representing the necessary energy to deform a sample to failure was obtained from the area under the stress-strain curve.

The cyclic compression test was similarly performed by loading the sample to 30% strain for 1600 cycles at 1 Hz. Energy absorption in cryogel was derived from the stress–strain relation during repeated loading and unloading cycles, which showed a hysteresis loop. During the hysteresis cycle, the area bounded within the hysteresis loop by the loading and unloading curves gave the dissipation energy (kJ/m^3) (energy absorbed due to the viscous properties of the cryogel). The percentage of energy dissipation (%) was calculated by dividing the dissipation energy with the area bounded between the loading curve and the horizontal axis, which represented the total energy applied during compression.

2.5. In vitro cell culture

2.5.1. Isolation and culture of BMSCs

Rabbit BMSCs were harvested and isolated according to standard procedures [22] and all experiments were approved by the Institutional Animal Care and Use Committee of Chang Gung University. Briefly, animals were anesthetized and 20 ml of bone marrow was drawn from a rabbit using a bone marrow aspiration needle fitted to a syringe containing 5 ml of heparin as an anticoagulant. Collected sample was diluted with an equal volume of PBS and centrifuged at 4 °C for 10 min at 1500 g. The supernatant was removed and the bottom layer was mixed with an equal volume of cell culture medium containing 20% FBS, 80% DMEM, 1% penicillin-streptomycin and 2 μg/ml fibroblast growth factor-2 (FGF-2). Centrifugation was repeated at the same condition and the supernatant was removed. The bottom layer dark-red solution was added to a T-75 flask containing 10 ml of cell culture medium and kept in a CO_2 incubator maintained at 37 °C. The cells were further sub-cultured in multiple flasks and cells at passages 3 or 4 were used for all studies.

2.5.2. Static cell culture

Disk-shaped crosslinked cryogel scaffolds (2 mm thickness × 8 mm diameter) were sterilized with 75% ethanol followed by UV exposure for 24 h and rinsed three times with PBS before being placed in a 24-well culture plate for cell seeding. An aliquot of 10 μl cell suspension (2×10^5 BMSCs/ml) was seeded onto one side of the scaffold and incubated in a CO_2 incubator at 37 °C for 2 h, followed by seeding 10 μl of the same cell suspension to the other side of the scaffold and incubated in a 37 °C CO_2 incubator for 2 h to allow cell adhesion. The cell-seeded scaffold was transferred to a new 24-well culture plate for separation from un-attached cells in the well. Cells culture in tissue culture polystyrene (TCPS) plates was taken as control. Both normal medium (NM) and osteogenic (OM) were employed for cell culture up to 28 days with medium change every three days. The NM consisted of 90% DMEM, 10% FBS and 1% penicillin-streptomycin whereas the OM was composed of 90% DMEM, 10% FBS, 1% penicillin-streptomycin, 0.1 μM dexamethasone, 50 μM L-ascorbic acid phosphate and 10 mM β-glycerolphosphate.

2.5.3. Dynamic cell culture

For dynamic cell culture, a Gn-EDC cryogel scaffold was used following the same sterilization and cell seeding procedures as described for static cell culture. The cell-seeded scaffold was cultured under compressive mechanical stimulation for 14 days in an ElectroForce® 5200 BioDynamic™ bioreactor containing 150 ml NM at 30 or 60% compression strain, 1 Hz frequency and 1 h/day stimulation duration [36].

2.5.4. DNA content and alkaline phosphatase (ALP) activity

The cell-seeded scaffold was removed from the culture plate and washed three times with PBS. For DNA content analysis, the scaffold was immersed in 1 ml digestion buffer solution (55 mM sodium citrate, 150 mM sodium chloride, 5 mM cysteine.HCl, 5 mM EDTA and 0.2 mg/ml papain) and shaken at 60 °C for 24 h. After centrifugation, 10 μl of

the supernatant was mixed with 200 μl bisBenzimide H 33258 solution (10 mg/ml) and the fluorescence intensity was determined at 365 nm excitation and 458 nm with an ELISA reader (Synergy HT, BioTek) [37].

For ALP activity, scaffolds were washed three times with PBS and immersed in 1 ml digestion buffer solution containing 55 mM sodium citrate, 150 mM sodium chloride, 5 mM cysteine HCl, 5 mM EDTA and 0.2 mg/ml of papain for 24 h at 60 °C. The solution was centrifuged and ALP activity in the supernatant solution was measured using an ALP kit (SensoLyte® pNPP ALP assay kit, AnaSpec, USA) at 405 nm using an ELISA reader and converted to mass using a standard curve. The specific ALP activity per cell basis was reported by normalizing the ALP mass with the DNA content (ng/μg).

2.5.5. Scanning electron microscopy/energy dispersive X-ray spectroscopy (SEM/EDS) analysis

After washing with PBS for three times, cells in the scaffold were fixed using 2.5% glutaraldehyde at 37 °C for 2 h and post-fixed with 1% OsO_4 (in 0.1 M phosphate buffer) at 37 °C for 3 h. After another three times PBS washing, the scaffold was dehydrated in increasing concentrations (50, 70, 80, 90, 95, and 100%) of ethanol. After complete drying by a critical point dryer, the sample was sputter coated with gold. Cell morphology and mineral deposition were examined by a scanning electron microscope (Hitachi S-3000N SEM, Japan). Energy dispersive X-ray spectroscopy (EDS) analysis was used to confirm mineral deposition and determine the elemental atomic percentage in the mineral deposit (HORIBA EX-250 EDS).

2.5.6. Live/dead and cytoskeleton staining

The qualitative evaluation of cell viability was assessed by a Live/Dead viability/cytotoxicity kit (Molecular Probes, USA). The scaffold was washed with PBS and stained with the Live/Dead staining solution containing 2 μM calcein AM (for live cells) and 5 μM ethidium homo-dimer-1 (EthD-1) (for dead cells) at 37 °C for 15 min. The morphology of cells was imaged under a Leica TCS SP2 confocal laser scanning microscope (excitation/emission 494/517 nm for live cells and 528/617 nm for dead cells).

For cytoskeletal staining, samples were fixed in 4%(w/v) paraformaldehyde in PBS for 30 min, followed by permeabilization in 0.1% Triton X-100 for 5 min. Before staining, the scaffold was washed with PBS and stained for actin cytoskeleton with 1% rhodamine phalloidin for 30 min in dark. After counter-stained with 0.1 μg/ml DAPI for cell nucleus for 5 min, the cytoskeletal arrangement was immediately visualized using a confocal laser scanning microscope (Leica TCS SP2) at excitation/emission wavelengths of 540 nm/570 nm for rhodamine phalloidin and 340 nm/488 nm for DAPI.

2.5.7. Immunofluorescence (IF) staining of COL I

Cells in the scaffolds were fixed in 4% paraformaldehyde in PBS for 30 min followed by PBST (PBS with 0.1% Tween 20) washing for 3 times, 15 min each. Nonspecific labeling was blocked with 1 ml of Hyblock 1-min Blocking Buffer (Goal Bio, Taiwan) and washed again with PBST. Collagen type I (COL I) primary antibody (1:200 in PBST, mouse monoclonal anti-COL I, Abcam, USA) was reacted with the sample for 24 h at 37 °C. Each sample was washed three times with PBST for 20 min each, followed by treating with Cy3-conjugated anti-mouse IgG secondary antibody (Jacksons Laboratories, USA) for 1 h at 37 °C. Another PBST washing was given prior to staining with 50 μg/ml DAPI for 15 min for nucleus and the sample was observed by a confocal laser scanning microscope (Leica TCS SP8) at excitation/emission wavelengths of 554 nm/559–713 nm for Cy3 and 405 nm/410–476 nm for DAPI. The semi-quantitative evaluation of COL I by IF staining was done through PAX-it!™ image analysis software.

2.5.8. Calcium and osteocalcin (OCN) quantification

Alizarin red S (ARS) was used to quantify the calcium ion content in mineralized ECM of BMSCs. The cell-seeded scaffold was removed from a culture plate and washed 3 times with PBS. After fixing with 2.5% glutaraldehyde solution for 1 h at 37 °C, the samples was reacted with 1 ml of ARS solution (2%(w/v) ARS in water, pH 4.1–4.3) for 1 h at room temperature. After several washes with water to remove excess dye, the sample was incubated with 1 ml of 10% cetylpyridinium chloride (CPC) solution to elute the ARS-calcium ion chelated complex. The absorbance of the solution was read at 540 nm in an ELISA reader (OD_{540}) and normalized with the DNA content.

The concentrations of OCN in cell-seeded scaffolds were determined by biochemical assays. Retrieved scaffolds were washed and immersed in digestion solution for 4 h (60 °C), followed by centrifugation to collect the supernatant. The OCN concentration was measured using a rabbit OCN ELISA kit (BlueGene Biotech., Shanghai, China) and quantified from a pre-determined standard curve.

2.5.9. Quantitative real-time polymerase chain reaction (qPCR)

The expression of osteogenic differentiation marker genes COL I, ALP, OCN and OPN was examined using standard protocols of RNA isolation and cDNA synthesis. TRIzol (Invitrogen, USA) was used to isolate RNA and the solution was transferred to a 1.5 ml microcentrifuge tube. The tube was vortexed for 15–30 s after adding 200 ml of chloroform to the cell suspension. The tube was placed in an ice bath for 5 min and centrifuged at 11000 rpm for 15 min. RNA was isolated from the supernatant layer and reacted with isopropanol in 1:1 ratio at −80 °C for 30 min. The supernatant was removed again and the solution was further centrifuged at 11000 rpm (4 °C) for 15 min. One milliliter of 75% ice cold ethanol was added and mixed at 4 °C for 10 min, followed by repeated centrifugation at 11000 rpm for 10 min each. The final supernatant solution was dried at room temperature and the RNA retrieved was dissolved in 30 ml of DEPC-treated water (Invitrogen) at 55 °C for 15 min. The RNA obtained (1 mg) was reverse-transcribed into cDNA using SuperScript III RNase H (Invitrogen). Glyceraldehyde 3-phosphate dehydrogenase (GAPDH) was used as the housekeeping gene. A SYBR Green RT-PCR kit (SYBR Green I Supermix, Bio-Rad) was used for quantitative real-time PCR (qPCR) measurements using a Mini Option detection system (Bio-Rad CFD-3120). The primer sequences were COL I (forward: TTCTATTGGTCCCGTCGGT; reverse: GCTGAGT CTCAGGTCGCG-3), ALP (forward: ATGATTTCACCATTCTTAGTACTG; reverse: TCAGAACAGGACGCTCAGGGG), OCN (forward: GACACCAT GAGGACCCTCTC; reverse: GCCTGGTAGTTGTTGTGAGC), OPN (forward: CACCATGAGAATCGCCGT; reverse: CGTGACTTTGGGTTTCTA CGC), GAPDH (GCTTTGCCCCGCGATCTAATGTTC; reverse: GCCAAAT CCGTTCACTCCGACCTT) [38].

2.6. In vivo studies

A critical size calvarial bone defect model in rabbit was used to evaluate bone regeneration by implanting BMSCs/cryogel constructs in rabbit skull. Animal protocols were approved by the Institutional Animal Care and Use Committee of Chang Gung University. Male New Zealand white rabbits weighing 3–4 kg were selected for the study and were kept in a single room and fed dried diet and water ad libitum. An intramuscularly injection of Atropin (0.3 mg/kg) was given, followed by general anesthesia using a mixture of Zoletil 50 (18 mg/kg) and Rompun 20 (1 mg/kg). The scalp was sterilized with betadine solution and a longitudinal incision was induced to create sub-periosteal dissection to expose the skull bony area. A surgical trephine of 10-mm diameter created two circular defect sites at the calvarial bone of the rabbit and bony discs were removed. A Gn-EDC cryogel scaffold (2 mm thickness × 10 mm diameter) was seeded with 1×10^6 BMSCs and dynamically cultured in an ElectroForce® 5200 BioDynamic™ bioreactor (with 150 ml NM) at 30% compression strain, 1 Hz frequency and 1 h/day stimulation duration for 14 days. The right defect created in the rabbit defect was filled with a cellular scaffold while an acellular cryogel was used to fill the left defect. Both defect sites were completely occupied by the samples and surgical sites were finally closed with 4-0

Ethicon sutures for post-operative care.

All animals were underwent computed tomography (CT) examination using a CT scanner (Somatom Sensation 16, Siemens) 1 and 8 weeks after implantation. The calvarial defect regeneration was analyzed by comparing both cellular and acellular sites, using OsiriX Image software (Pixmeo, Bernex, Switzerland) for 2D coronal and 3D views. All animals were euthanized at 16 weeks post-operation, using lethal doses of pentobarbital (0.5 g per kg body weight) and the implants were dissected out for gross evaluation. All samples were fixed in 10% formaldehyde, dehydrated and embedded in paraffin to make 10-mm slice sections. Samples were subjected to hematoxylin and eosin (H&E), Masson's trichrome and immunohistochemical (IHC) staining of COL I and OCN following standard protocols. Bone regeneration in cellular scaffolds in comparison with acellular ones was assessed by recording the images under an inverted optical microscope (Olympus IX-71).

2.7. Statistical analysis

All quantitative data were expressed as mean ± standard deviation (SD) and one-way ANOVA LSD test was used to determine the significant difference.

3. Results and discussion

3.1. Characterization of cryogel scaffolds

3.1.1. Physico-chemical properties

By combining ceramic nanoparticles (nHAP) with an organic polymer (gelatin), we aim to improve the osteo-inductive properties and mechanical properties of gelatin by designing a composite cryogel scaffold to enhance its applicability for bone tissue engineering [39]. As dominance of nHAP in the composite might lead to weakening of the scaffolds, we fixed the gelatin/nHAP mass ratio at 2/1 to study the effect of crosslinking agent on the properties of cryogels [22]. The optimum composition of gelatin/nHAP is expected to coincide with the slow degradation characteristics and mechanical properties requirement for a bone tissue engineering scaffold through chemical crosslinking of gelatin with EDC or GA. Considering the crosslinking agents for cryogel synthesis, GA is a longer crosslinker than EDC (a zero-length crosslinker) and has faster reaction kinetics [40]. However, GA was reported to cause local toxicity at the implantation site owing to the release of unreacted aldehydes [41].

From the SEM images, macroporous morphology with open interconnected pores with pore size ranging from 50 to 120 μm was observed for cryogel scaffolds (Fig. 1). This pore size and pore morphology could meet the requirements for scaffolds intended for bone tissue engineering. From elemental analysis through EDS shown in inserts of Fig. 1, composite cryogels show strong Ca and P peaks with a Ca/P ratio value of 1.59 for Gn-EDC and 1.69 for Gn-GA. The Ca/P ratios are comparable to the theoretical value of HAP (1.67) and confirm the incorporation of nHAP in gelatin-based cryogel scaffolds.

Additional experiments with capillary flow porosimetry provided the average pore size of cryogel scaffolds (Table 1). The average pore size and porosity did not show significant dependence on the presence of nHAP or the type of crosslinking agent used (i.e. EDC or GA). In tissue engineering, an adequate porous structure of the scaffold is very important to allow cellular penetration into the construct. Apart from that, it is also necessary for waste and nutrient transports. Our experiments confirmed that the mean average pore size of all scaffolds is ideal for penetration and proliferation of BMSCs, while higher than 80% porosity is expected to be beneficial for cell ingrowth and survival [18].

The degree of crosslinking was above 80% for every scaffold and no significant difference was found when using different crosslinking agents. It should be noted that the degree of crosslinking was calculated based on the number of free amine groups in gelatin. The aldehyde group in GA will react with amino groups of lysyl and hydroxylysyl

residues in gelatin coupled with the release of a water molecule, after which imines (Schiff base intermediates) will be formed and react further to form larger crosslinked entities. In contrast, EDC as a zero-length crosslinker links amine and carboxyl groups of proteins by activating the carboxylic acid group of glutamic and aspartic amino acid of a protein molecule to form an amine-reactive O-acylisourea intermediate. Although EDC consumes only one amine group compared to GA that consumes two, it still efficiently crosslinked the matrix and showed high degree of crosslinking. This could be explained from the fact that the amount of glutamic and aspartic amino acid was reported to be 3.7 times that of lysine and hydroxylysine in porcine skin gelatin (12.81 vs. 3.46 μmol/g ash-free protein) [42]. Nonetheless, there was significant decrease of degree of crosslinking when nHAP was added (Table 1). This should be due to the steric hindrance caused by entrapped nHAP, which might cause screening of the effective covalent crosslinking of gelatin macromolecules in a composite cryogel and lead to reduced crosslinking efficiency.

Swelling ratio in water is considered as an important feature to be evaluated for a scaffold designed for tissue engineering applications. Swelling will increase the pore size and the surface area to volume ratio of the scaffold and thereby facilitates the infiltration of cells into the 3D scaffold [43]. Moreover, since the gelatin scaffold is made up of crosslinked polymer chains embedded with ceramic constituents; its efficiency in water absorption would be a direct measure of pore-size mediated cellular infiltration as well as fluid absorption both in vitro and in vivo. The swelling behavior of scaffolds was measured through water immersion and the swelling ratio is shown in Table 1. Gelatin cryogel crosslinked with EDC had the highest swelling ratio among all scaffolds. Incorporation of nHAP led to significantly lower swelling ratio for both EDC and GA-crosslinked cryogels. However, unlike the insignificant effect of crosslinking agent on degree of crosslinking, the swelling ratio of GA-crosslinked cryogels were significantly lower than that of EDC-crosslinked cryogels for both G and Gn cryogels. We postulate that the difference in ionic carboxyl and amine groups in the crosslinked cryogel may play a role in influencing the swelling ratio, which might due to the different crosslinking mechanism between EDC and GA.

The in vitro degradation of cryogels in PBS and collagenase solutions at 37 °C is another important cryogel property, which determines the stability of a cryogel scaffold under physiological relevant conditions. PBS degradation is relevant due to the abundance of water in human body while collagenase specifically imitates enzymatic response of the cryogel in vivo. Collagenase is a protease that cleaves the bond between a neutral amino acid (X) and glycine in the sequence Pro-X-Gly-Pro, which is found abundantly in collagen and gelatin. The degradation studies using PBS and collagenase could thus mimic the possible deterioration of cryogels in aqueous solutions as well as in vivo. Compared to collagenase solutions, samples in PBS show much slower degradation rate as expected, with Gn-GA displayed the highest resistance to degradation (Fig. 2). All samples in PBS or collagenase show similar trends of degradation profiles with Gn > G, indicating faster hydrolysis rate of composite cryogels. The nHAP embedded in the crosslinked gelatin matrix in the composite cryogel may interrupt physical entanglements of gelatin polymer chains in the gel matrix and thereby lead to faster degradation rates in PBS and collagenase in accordance with lower values of degree of crosslinking (DC) in Table 1. Nonetheless, not in line with the trend observed for DC where insignificant difference was found using different crosslinking agents, EDC crosslinked cryogels showed much faster degradation rates compared to GA crosslinked ones (Fig. 2). This trend is consistent with a previous report using GA and EDC to crosslink electrospun collagen scaffolds, where collagen scaffolds treated with EDC were found to retain lower structural stability than GA [44]. Therefore, the degradation rates of cryogels calculated from weight loss should not be solely correlated to DC that measures the free amino groups. It may be related to the higher hydrolytic stability of imine linkages produced by GA crosslinking
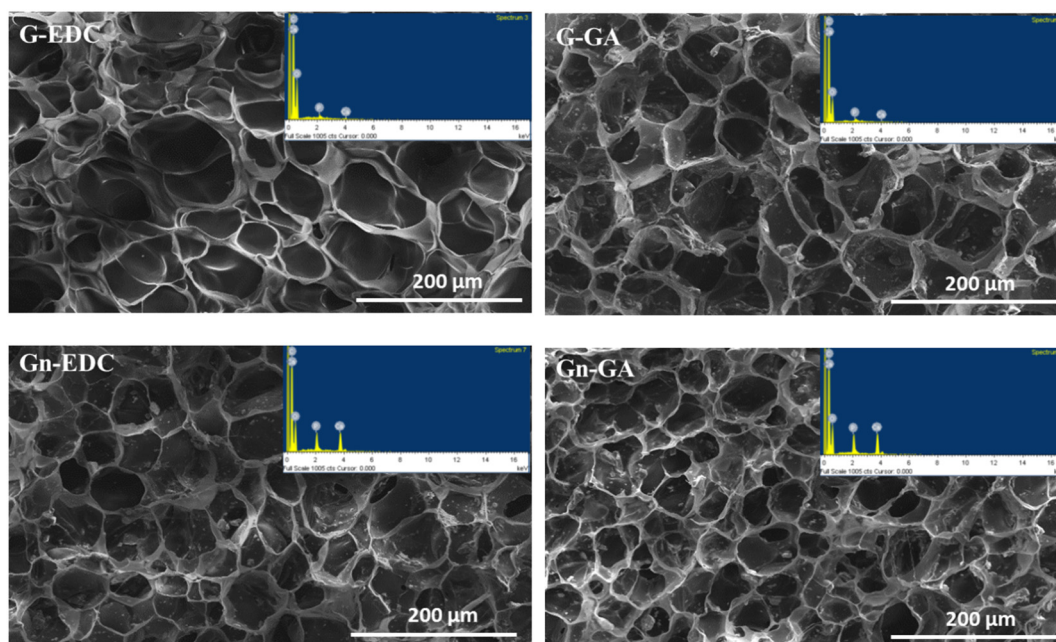
Fig. 1. Scanning electron microscope (SEM) images of gelatin (G) and gelatin/nanohydoxyapatite (Gn) cryogel prepared by using EDC or glutaraldehyde (GA) as the crosslinking agent (bar = 200 μm). The inserts are EDS spectra.

compared to the relatively more hydrophilic amide linkages by EDC crosslinking.

3.1.2. FTIR and XRD

FTIR was used to characterize the functional groups present in G and Gn cryogels to ensure the presence of nHAP in composite cryogels. As shown in Fig. 3A, pure gelatin shows characteristic amide I peak at $1654 \, cm^{-1}$ and amide II peak at $1517 \, cm^{-1}$, which is consistent with the peaks observed in G and Gn. In a similar fashion, absorption bands of pure nHAP is correlated with its presence in Gn cryogels from the presence of carbonate peak at $877 \, cm^{-1}$, phosphate stretching vibrations at 580 and $609 \, cm^{-1}$ and hydroxyl bands at 1471, 1417 and $3429 \, cm^{-1}$ [45]. All results thus cross-confirm the presence of nHAP in composite gelatin cryogels.

In addition to FTIR, the presence of nHAP in composite cryogels was further examined through the identification of crystalline peaks of the ceramic counterpart by XRD analysis (Fig. 3B). The spectrum showed a semi-crystalline peak at 21.5° for gelatin, which was also displayed by G regardless of the crosslinking agent used. However, the intensity of the peak at 21.5° reduced to a minor broad distribution when gelatin was combined with nHAP to form composite cryogels [46]. Along with the minor gelatin peak, Gn cryogels showed all characteristic crystalline peaks assigned to nHAP at 25.9°, 32.2°, 33.3°, 34.2°, 40.2°, 46.9°, 49.7° and 53.3° 2θ values. The reduction in the intensity of the gelatin peak in Gn cryogels is due to the screening effect from strong nHAP peaks, as mentioned in earlier literatures [45]. In short, the physico-chemical characterizations validate the formation of composite cryogel scaffolds through nHAP incorporation.

3.1.3. Mechanical properties

As shown in Fig. 4A and B, compressive stress-strain curves of all cryogels could be fitted satisfactorily with the empirical non-linear model shown in Eq. (4). The elastic modulus calculated from the slope of the stress-strain curves at 30% strain, which represents the initial linear region, was found to be significantly increased using either GA as the crosslinking agent (*i.e.* G-GA > G-EDC, Gn-GA > Gn-EDC) or by incorporating nHAP (*i.e.* Gn-EDC > G-EDC, Gn-GA > G-GA) (Table 2). A similar trend was also observed for the ultimate strain, ultimate stress and toughness. Compared with the elastic moduli of gelatin cryogels embedded with HAP particles and crosslinked with oxidized dextran (18.5 kPa), our scaffolds are much stronger and is expected to be suitable for tissue-engineering of non-load-bearing bones such as in the craniofacial area [47]. Overall, the mechanical properties of Gn-GA were significantly better than those of other cryogels. This could be ascribed to the fact that nHAP are present in the cryogel strut, resulting in higher resistance to mechanical compression compared to the brittle nature of G samples. For cryogels crosslinked with different crosslinking agents, the higher network integration of GA-crosslinked cryogels is consistent with their slower degradation rates in both PBS and collagenase (Fig. 2).

The mechanical requirements of bone tissue engineering scaffolds are complex, where compressive, tensile and fatigue properties are all required for load bearing [48]. In general, bone tissue engineering scaffolds made from natural polymers (*e.g.* gelatin) have sub-optimal mechanical properties even after crosslinking [49]. Thus, they are insufficient to be used as a load-bearing scaffold for bone regeneration compared to metallic and ceramic materials. Combining natural
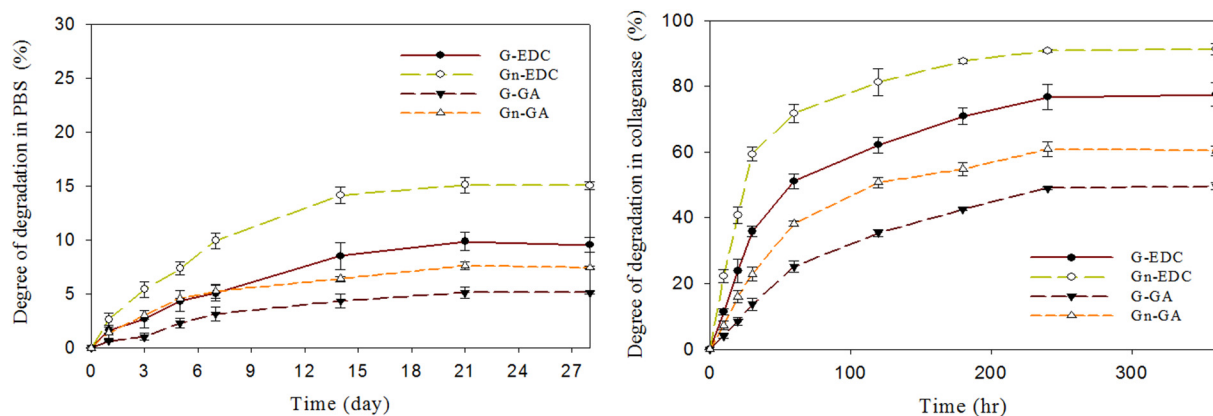
Table 1
The average pore size, porosity, degree of crosslinking (DC) and swelling ratio (SR) of cryogel scaffolds. Values are mean ± SD of six independent measurements.

	EDC				GA			
	Pore size (μm)	Porosity (%)	DC (%)	SR	Pore size (μm)	Porosity (%)	DC (%)	SR
G	55.0 ± 4.7	87.9 ± 2.4	87.7 ± 0.3	10.6 ± 0.6	58.3 ± 5.0	85.8 ± 1.2	88.6 ± 0.3	7.2 ± 0.1[#]
Gn	50.0 ± 6.9	83.0 ± 2.4	84.4 ± 0.2[*]	6.3 ± 0.4[*]	52.8 ± 7.6	81.0 ± 2.3	85.2 ± 0.5[*]	5.4 ± 0.4[*,#]

[*] $p < 0.05$ compared with cryogels crosslinked with the same crosslinking agent but without nHAP.
[#] $p < 0.05$ compared with cryogels of the same composition but crosslinked with different crosslinking agent.

Fig. 2. Degradation of cryogels in PBS and collagenase solutions.

polymers with more robust materials such as bioceramics (*e.g.* nHAP) to create composite scaffolds may address these limitations. However, composite cryogels still lack mechanical strength to be evaluated for regeneration of segmental bone but could be considered for regeneration of calvarial or cancellous bones [50]. Indeed, due to the compliant mechanical properties of the G or Gn scaffolds, they are best suited for non-load-bearing indications such as craniofacial repair [51]. Nonetheless, as many bone fractures require fixation in combination with bone grafting, a compliant G or Gn scaffold could theoretically be applied in a load bearing application when combined with mechanical fixation [52]. Additionally, similar to formation of rigid bone from the soft cartilaginous callus during bone fracture healing, it is also possible that G or Gn scaffold could produce a graft that quickly fills the bone defect to supersede their poor mechanical properties for bone tissue engineering application.

From Fig. 5, the cyclic compression testing of cryogels at 30% strain and 1 Hz shows a hysteresis loop in the stress–strain curves of all cryogels. The dissipation energy is the amount of mechanical energy dissipated and could be calculated from the area enclosed in the hysteresis loop. From Table 2, the dissipation energy and the percentage of energy dissipation of G-EDC was not statistically different from that of G-GA. Nonetheless, Gn-GA displayed significantly higher dissipation energy and percentage of energy dissipation than G-GA and Gn-EDC, making it to dissipate the highest energy during compression and to perform better than other cryogels in terms of energy dissipation. Furthermore, cyclic compression loading-unloading curves during the first cycle and all subsequent cycles appeared to be reversible and reproducible, which endowed cryogels with an unique property to be fully recovered from compressive loading–unloading cycles without

causing permanent bond breakage even at 30% strain (Fig. 5). Indeed, the tough nature of a cryogel scaffold rendered the scaffold to absorb impacts without permanent damage and recover back to its original form even after experiencing large successive compressive force and deformation. That Gn-GA had the highest energy dissipation throughout the cyclic compressing is consistent with our previous study [53] as well as with other reported findings [54], where it was shown that under an identical dynamic compression, the dissipation energy of a scaffold crosslinked with higher amount of crosslinker or with a crosslinker that produces denser network will be much higher. Therefore, incorporation of nHAP in cryogels will have a positive impact on energy dissipation during cyclic compression, revealing the higher mechanical stability of the composite scaffolds in load bearing application. This unique feature contributes to the development of composite cryogels as tough scaffolds for bone tissue engineering, which can recover from large strains and absorb impacts without permanent damage. Most importantly, this property will facilitate dynamic cell culture using a cryogel scaffold when subject to cyclic compressive loading-unloading in a bioreactor. We will take advantage of this unique feature later in this study.

The superior recovery property of cryogel from large strains was further analyzed from the enclosed area of the hysteresis loops during the successive loading–unloading cycles at 30% maximum strain and the calculated dissipation energy during 100th, 200th, 400th 800th and 1600th cycles are compared in Fig. 6. The cryogels crosslinked by EDC (G-EDC and Gn-EDC) did not show significant difference in dissipation energy among all cycles. Nonetheless, cryogels crosslinked by GA (G-GA and Gn-GA) showed slightly but significantly lower dissipation energy during successive compression cycles, indicating EDC-
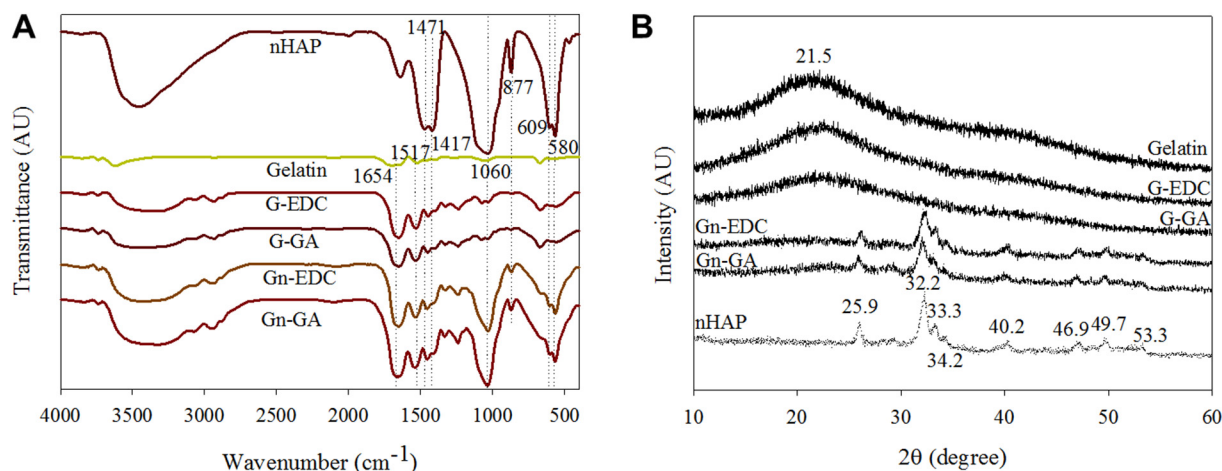

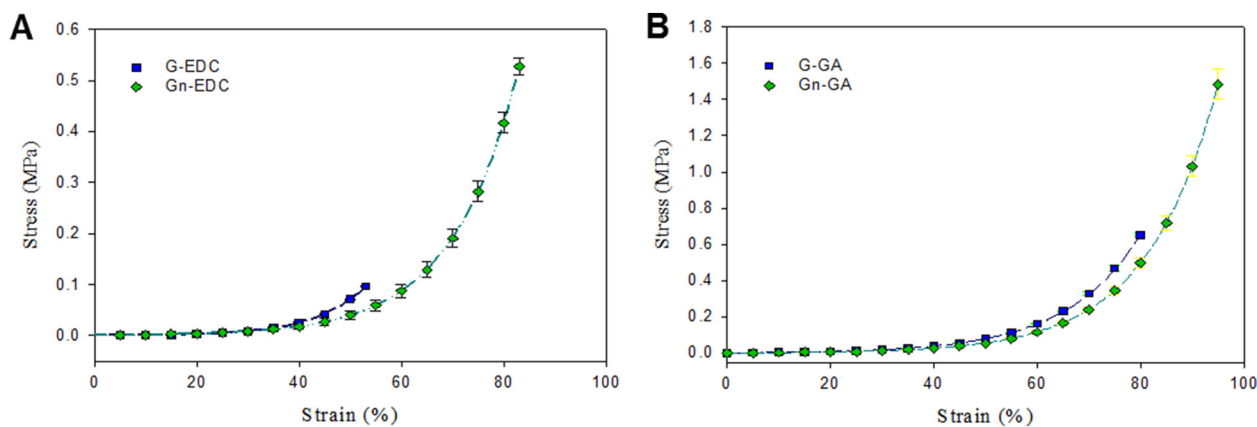**Fig. 3.** The characterization of cryogels through FTIR (A) and XRD (B) analysis.

Fig. 4. The compressive stress-strain curves of G and Gn cryogels prepared through EDC (A) or GA crosslinking (B).

crosslinked gelatin network may be more stable in the presence of successive compressive force that may lead to irreversible breakage of bonds in the crosslinked polymer networks.

3.2. In vitro cell culture-static culture

3.2.1. Cell proliferation and ALP activity

Since nHAP was reported to be a weak osteo-inductive material [55], we used normal medium (NM) as well as osteogenic medium (OM) to compare the *in vitro* cellular response of BMSCs in G and Gn cryogel scaffolds (Fig. 7A). In NM, the same cell number on day 0 (4 h) for all groups indicates excellent cell attachment efficiency in 3D cryogel scaffolds comparable to theoretically quantitative cell attachment on TCPS. This observation could be supported from similar pore size and pore structure among all cryogels in Fig. 1 and Table 1. Nonetheless, less DNA content was found for Gn cryogels compared to G cryogels and TCPS controls with TCPS groups consistently having higher cell numbers as culture time progresses, indicating BMSCs on TCPS or in G had higher cell proliferation rate than in Gn.

The effect of OM over NM in reducing the cell proliferation rate was further verified in Fig. 7A. Overall, the Gn groups exhibited the lowest cell proliferation rates among all groups in OM. Multiple rationales could be inferred by using OM for culture of BMSCs [56]. Nonetheless, the reduction of total DNA content in OM as well as the lower cell number in Gn inferred better osteogenic differentiation of BMSCs [57]. The influence of OM validates the effects of osteo-inducing factors in the medium on BMSCs, which could be further enhanced by using Gn cryogels by taking advantage of the osteoinductive properties of nHAP. The crosslinking agent also significantly affected cell proliferation rate; EDC-crosslinked cryogels always had lower cell number than GA-crosslinked ones, regardless of cryogel composition. Therefore, BMSCs cultured in Gn-EDC cryogels had the lowest cell numbers throughout the culture period. Overall, the cell proliferation studies suggest that by incorporating nHAP and using different crosslinking agents during cryogel preparation, chemical cues generated therewith will synergistically influence the cellular response of seeded BMSCs.

The DNA content observed in different cryogels could be further correlated with the ALP activity of BMSCs (Fig. 7B). The ALP marker is used to identify the initiation of mineralization through nucleation of inorganic phosphates with Ca^{2+}, which results in calcification within local environment. The hydrolysis of phosphate esters by ALP leads to elevation of mineralization of ECM and regulation of downstream cell differentiation factors to initiate osteogenic differentiation [58]. Thus, ALP can be considered as an effective measurement tool for the differentiation of BMSCs into the osteogenic lineage. The normalized ALP activities of BMSCs cultured on TCPS and in cryogels are reported in Fig. 7B using NM or OM for cell culture. Even in NM, Gn cryogels exhibited higher ALP activities throughout the culture period; especially during the first 14 days. As shown from cell proliferation rates in Fig. 7A, Gn-EDC showed significant reduction in cell number compared with Gn-GA on day 7 and 14. This trend could be correlated well with concomitant higher ALP activities for Gn-EDC. Indeed, the ALP activity of Gn-EDC was 4.39, 3.70, 3.61, 1.84, 1.49 and 1.51 folds that of Gn-GA on day 0, 3, 7, 14, 21 and 28, respectively. A higher ALP value in the early period of cell-culture supports the osteogenic differentiation of BMSCs. In addition, the higher ALP activity of G-EDC (Gn-EDC) over G-GA (Gn-GA) reveals the advantage of using EDC for crosslinking gelatin cryogel scaffolds for differentiation of BMSCs towards the osteogenic lineage. When NM was replaced with OM, Gn cryogels displayed a drastic increase in ALP activity while G cryogels had comparable values. On day 14, Gn-EDC cryogel cultured in OM showed the highest ALP activity due to the synergistic effect of nHAP and the crosslinking agent as ALP is a characteristic early marker of osteogenesis [22].

3.2.2. Cell morphology and mineralization

EDC and GA-crosslinked Gn cryogels cultured with BMSCs for 14 and 28 days in both NM and OM were assessed by SEM/EDS (Fig. 8). The process of mineralization of ECM due to of stem cell differentiation could be estimated both quantitatively and qualitatively. Inorganic calcium phosphate deposition occurs at the middle of the cell

Table 2

The mechanical properties of cryogel scaffolds. Values are mean ± SD of six independent measurements.

	G-EDC	Gn-EDC	G-GA	Gn-GA
Elastic modulus @30% strain (kPa)	65.9 ± 15.4	94.1 ± 5.1[*]	95.2 ± 9.81[#]	138.6 ± 2.7[*,#]
Ultimate strain (%)	53.3 ± 0.6	83.3 ± 0.6[*]	80.3 ± 1.8[#]	99.7 ± 0.6[*,#]
Ultimate stress (kPa)	97.7 ± 3.2	523.8 ± 26.1[*]	700.9 ± 58.2[#]	1941.0 ± 114.7[*,#]
Toughness (kJ/m³)	9.8 ± 0.5	69.3 ± 5.8[*]	96.7 ± 10.4[#]	286.2 ± 21.0[*,#]
Initial dissipation energy (kJ/m³)	0.50 ± 0.02	0.58 ± 0.03[*]	0.52 ± 0.02	1.14 ± 0.01[*,#]
Initial percentage of energy dissipation (%)	28.89 ± 3.97	30.66 ± 3.31[*]	32.08 ± 2.82	40.07 ± 1.81[*,#]

[*] $p < 0.05$ compared with cryogels crosslinked with the same crosslinking agent but without nHAP.

[#] $p < 0.05$ compared with cryogels of the same composition but crosslinked with different crosslinking agent.
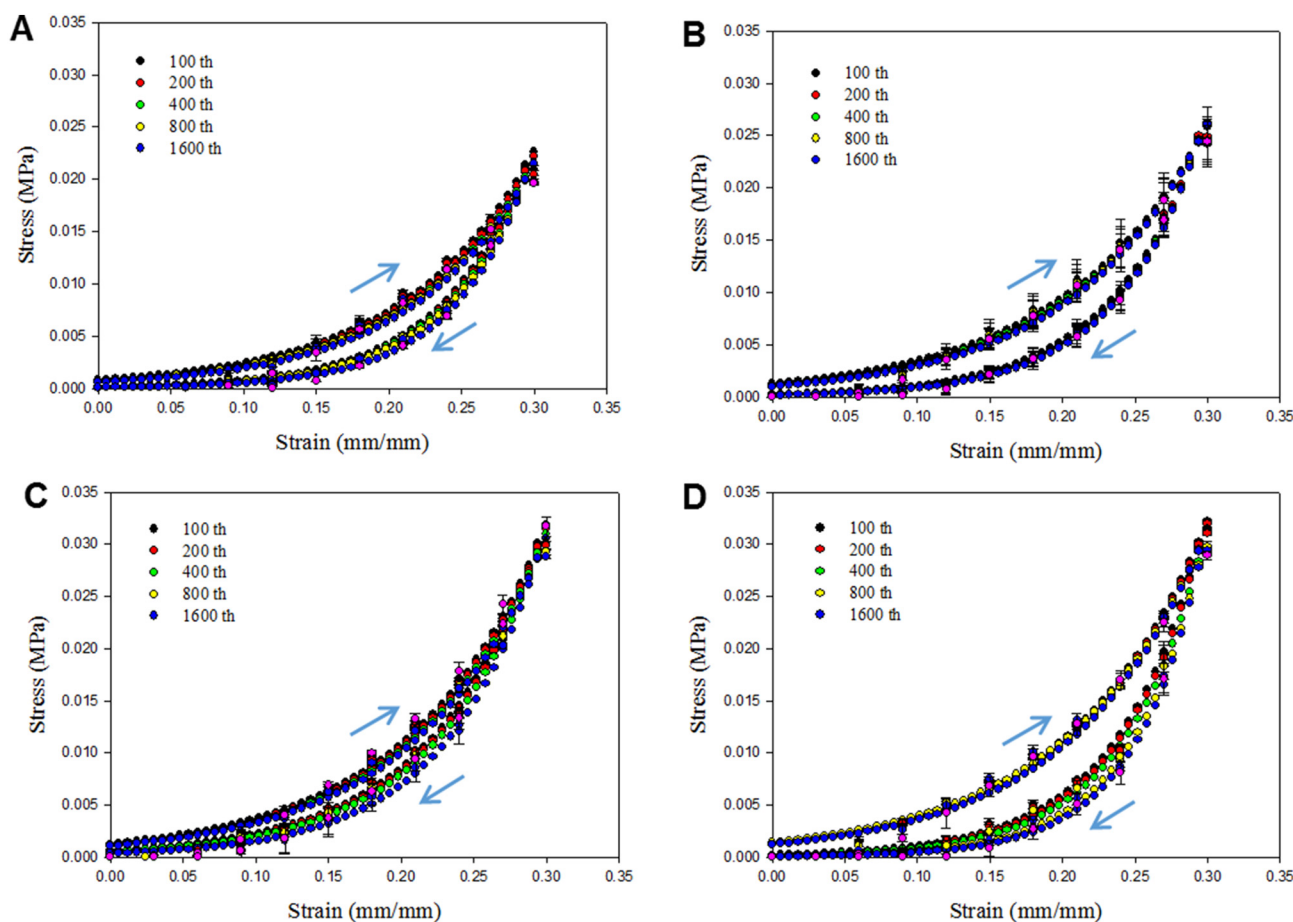
Fig. 5. The compressive loading-unloading hysteresis curves during 1600 successive compression to a maximum strain of 0.3 for G-EDC (A), Gn-EDC (B), G-GA (C) and Gn-GA (D) cryogels.

differentiation period and thus it could be considered as a proof of osteoblast formation [59]. The SEM observation could be taken as a qualitative tool for cell morphology and mineralization while EDS analysis is useful to determine the atomic percentages of elements present in the deposited mineral during osteogenic differentiation [60]. From Fig. 8, mineralized nodules were clearly visible within cryogels on day 14. In NM, cells in G cryogels displayed intermix of slightly rounded and spread cell morphology with visible porous cryogel background. Gn showed similar cell appearance, but the ECM appeared to be more mineralized judging from the white dots in the SEM images due to the osteoinductive nature of nHAP even without osteogenic

factors in NM (Fig. 8). These small white depositions observed in Gn are due to the early deposition of calcium phosphate in the form of hydroxyapatite.

Interestingly, all cryogels on day 28 had well spread cell morphology due to cell differentiation, which resulted in complete filling of 3D pores in a cryogel scaffold. A much thicker layer of BMSCs spreading in G should be due to the higher cell proliferation rate in G compared to Gn cryogels as shown before from DNA quantification. This was verifiable from more visible scaffold pores in Gn cryogels in the SEM images. The mineral deposition was much more pronounced in Gn than G on day 28 as mineral production is a late osteogenic differentiation
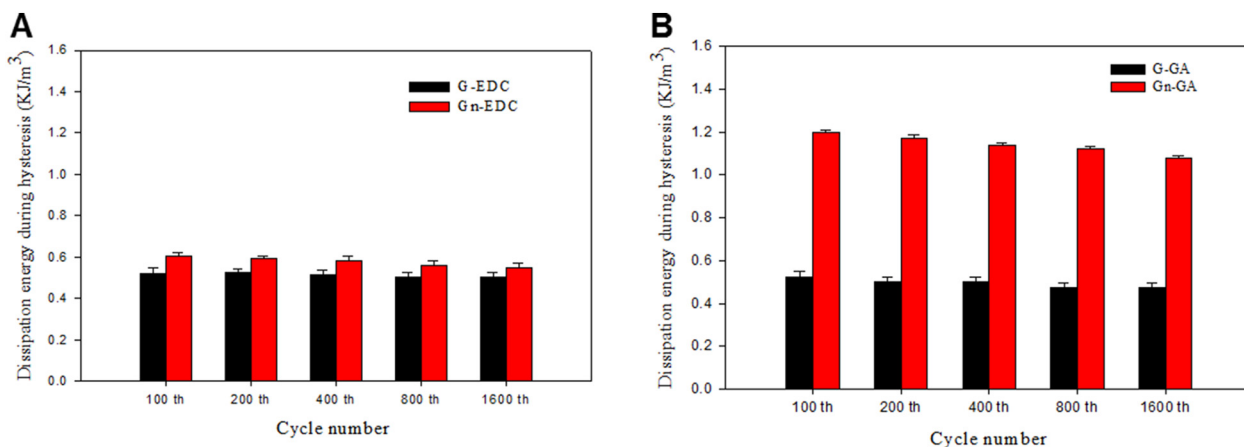
Fig. 6. Dissipation energy of EDC-crosslinked (A) and GA-crosslinked (B) cryogels during successive compression cycles.
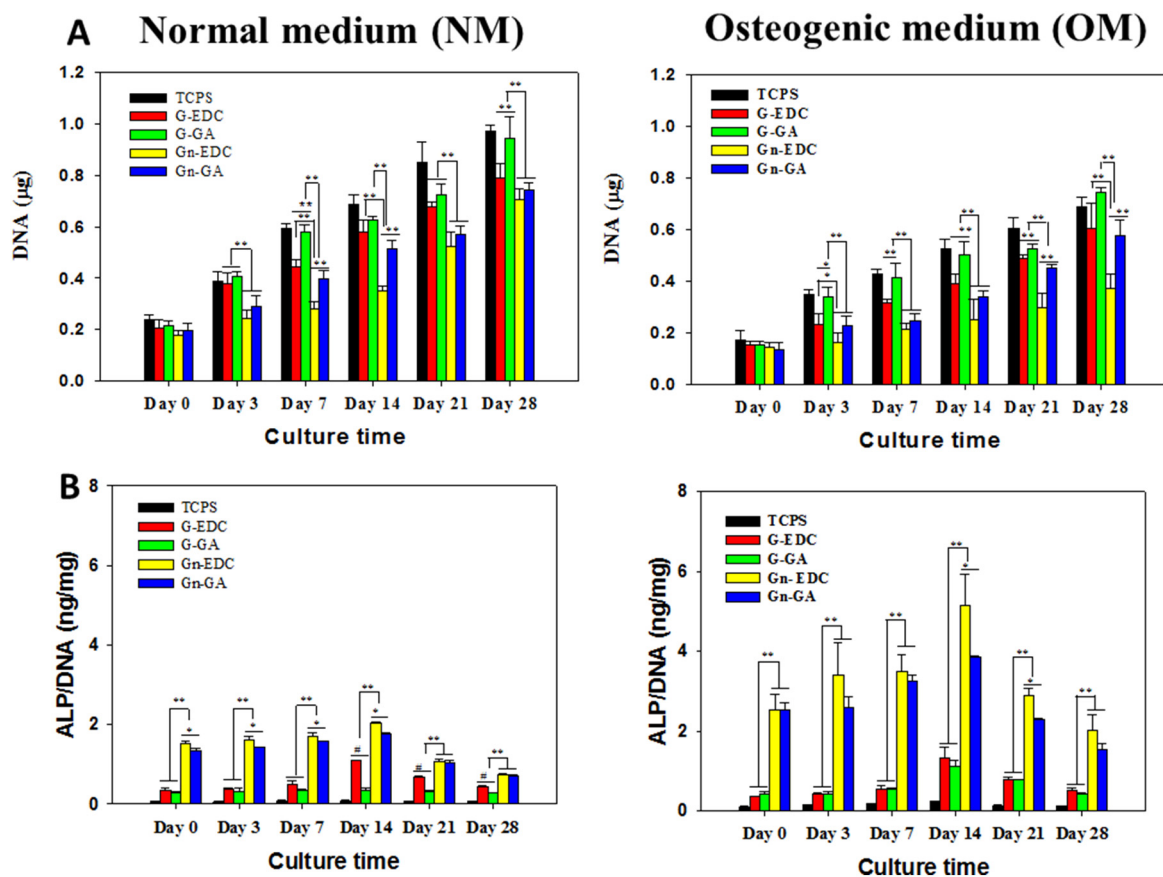
Fig. 7. The DNA content (A) and normalized alkaline phosphatase (ALP) activity when BMSCs (B) were cultured on TCPS and in different cryogels using normal medium (OM) and osteogenic medium (OM). *$p < 0.05$, **$p < 0.01$.
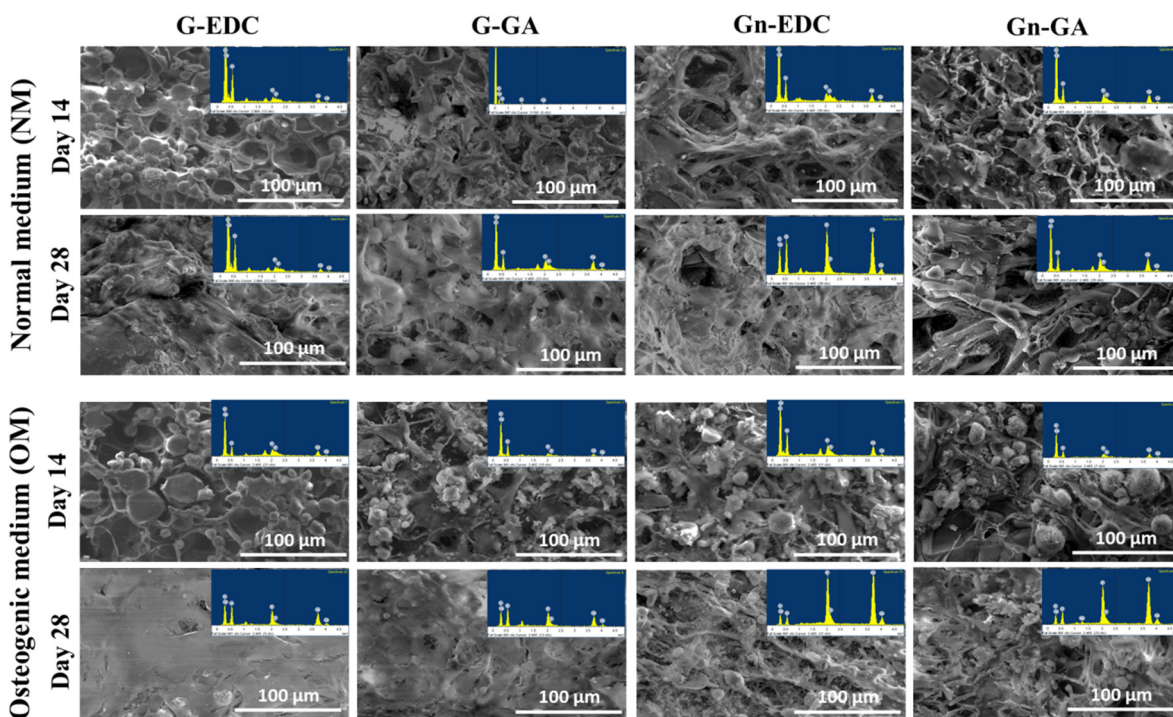

Fig. 8. Scanning electron microscopy/energy dispersive X-ray spectroscopy (SEM/EDS) analysis of the morphology and mineralization of BMSCs when cultured in different cryogels using normal medium (MM) and osteogenic medium (OM).

Table 3
The elemental composition analysis when BMSCs cultured in different cryogels for 14 and 28 days by SEM/EDS analysis.

		Normal medium (NM)				Induction medium (OM)			
	Element	G-EDC	Gn-EDC	G-GA	Gn-GA	G-EDC	Gn-EDC	G-GA	Gn-GA
14 days	C	73.6%	76.1%	72.0%	75.1%	73.3%	72.11%	69.5%	67.1%
	O	25.3%	21.9%	27.4%	23.3%	24.1%	25.18%	29.4%	30.1%
	Ca	0.63%	1.20%	0.32%	0.99%	1.31%	1.73%	0.59%	1.59%
	P	0.52%	0.77%	0.26%	0.64%	1.26%	1.11%	0.52%	1.04%
	Ca/P ratio	1.21	1.56	1.23	1.55	1.04	1.56	1.13	1.53
28 days	C	55.9%	45.5%	72.8%	68.7%	53.8%	46.3%	49.3%	40.2%
	O	39.3%	43.2%	24.3%	26.8%	39.9%	27.6%	44%	38.0%
	Ca	2.49%	6.45%	1.66%	2.57%	3.33%	15.9%	3.44%	12.9%
	P	2.31%	4.84%	1.24%	1.89%	2.92%	10.17%	3.26%	8.41%
	Ca/P ratio	1.08	1.33	1.34	1.36	1.14	1.56	1.06	1.52

marker with the cell morphology to become more spread. Indeed, BMSCs tended to mineralize through differentiation than proliferation in Gn cryogels as shown from their elevated ALP activity in Fig. 7B. Similar to previous analysis, the synergistic effect on cell mineralization due to nHAP and OM is observed in all cryogel scaffolds. Taken together, both DNA and ALP quantification in Fig. 7 coincide with cell morphology and mineralization from SEM/EDS analysis in Fig. 8.

The quantitative estimation of mineralization through Ca/P atomic ratio was further confirmed through EDS (Table 3). The respective EDS spectrum detected the presence of C, O, Ca and P elements in the mineral deposits but with distinctive scaffold-dependent features. The highest levels of Ca and P were detected for Gn-EDC irrespective of culture medium used. The cortical bone contains calcium phosphate in the form of hydroxyapatite with an ideal Ca to P ratio of 1.67. Therefore, a similar ratio of mineral deposition is much preferable for ideal bone regeneration. The measured Ca/P ratios of G-EDC, G-GA, Gn-EDC and Gn-GA in NM were 1.21, 1.23, 1.56 and 1.55, respectively, while it were 1.04, 1.13, 1.56 and 1.53 in OM after 14 days. Irrespective of culture medium, all Gn cryogels had higher Ca/P ratios than G cryogels and approaching the ideal stoichiometric ratio of 1.67. A similar trend was observed on day 28, where G-EDC, G-GA, Gn-EDC and Gn-GA displayed respective Ca/P ratios of 1.08, 1.34, 1.33, 1.36 for NM and 1.14, 1.06, 1.56 and 1.52 for OM. A lower Ca/P ratio on day 28 may be due to leaching of Ca^{2+} ions from the cryogel surface during medium change. Nonetheless, the closer Ca/P ratio of Gn over G cryogels at both time points endorsed the suitability of Gn cryogels as bone tissue engineering scaffolds, with culture in OM could further accelerating the osteogenic differentiation of BMSCs.

3.2.3. Quantification of calcium and osteocalcin (OCN)

The calcium deposition observed in various cryogels was critically analyzed for the effect of nHAP, crosslinking agent and culture medium. Calcium deposition by BMSCs initiates at the later stages of the cell proliferation cycle and in vitro cell culture duration is much critical in the process of calcium deposition [61]. The calcium ions on cell surface attached to ARS when cryogels were stained with an ARS solution through a chelation process to form ARS−Ca^{2+}. In further treatment with CPC, the extracted ARS−Ca^{2+} complex in the extraction medium showed an absorbance value (OD_{540}) to provide a direct estimation of the extent of mineralization after normalizing with the DNA content (μg). The calcium quantification from mineralization of BMSCs in various cryogels on day 14, 21 or 28 demonstrates the influence of OM over NM in accelerating differentiation of BMSCs (Fig. 9A).

G-EDC and G-GA cryogels showed no significant difference in normalized calcium content throughout the culture period in NM and OM. Nonetheless, the calcium content of Gn-EDC was significantly higher than Gn-GA. Furthermore, the calcium content of Gn was also significantly elevated compared with G. Two scenarios could be suggested to be responsible for the difference in calcium deposition. One is the combined effect of incorporating nHAP and using EDC as the crosslinking agent, which led to higher mineralization and calcium deposition. The other is the action of inductive factors in OM, which further enhanced the osteogenic differentiation of BMSCs. These are also in line with higher ALP activity (Fig. 7) and more mineral deposition from SEM/EDS (Fig. 8). Similar to previous assumptions, the calcium content measurement announced the superior performance of Gn-EDC cryogel over others as a scaffold for osteogenesis of BMSCs.

The protein concentration of OCN, a marker protein for the bone formation process, was shown in Fig. 9B. The normalized values of OCN on day 7 was similar in NM and OM with no significant difference among all cyogels. Longer durations to 14 and 28 days resulted in more OCN production with higher values in OM than NM. Gn-EDC supported the maximum OCN secretion from BMSCs on day 14 and 28 in both culture media. Similarly, Gn-GA had the second highest OCN, with substantial increase of normalized OCN values from day 7 to 28. Interestingly, G-EDC had higher OCN content than that of G-GA on day 14 in NM as well as on day 14 and 28 in OM, which could be correlated with the higher cell proliferation rate and lower cell differentiation rate of BMSCs in G-GA. Being a late stage marker during osteogenic differentiation of BMSCs [62], OCN quantification thus re-assures the advantage of Gn-EDC cryogel over other samples and declares the effect of nHAP-OM synergy in BMSC osteogenesis.

3.2.4. Osteogenic gene expression

A crucial evidence of BMSC differentiation is the identification of relevant osteogenic markers during in vitro cell culture. While undergoing differentiation, BMSCs undergo three different processes called proliferation, maturation and mineralization, which regulate the up-down expression of various marker genes during early, mid and later stages of cell differentiation [63]. Depending on the substrate and culture environments, the intensity and expression of each marker varies from one to another. ALP, COL I, OCN and OPN are considered the major osteogenic differentiation marker genes with ALP and COL I being the early differentiation markers while OCN and OPN expressed at mid-later stages of BMSC osteogenic differentiation [64].

The relative mRNA expressions of BMSCs in different cryogels in NM and OM are shown in Fig. 10. The ALP expression started to increase on day 3 and further elevated to reach a maximum on day 14 irrespective of culture medium. Similar to previous results, Gn-EDC had the highest ALP gene expression in both media while G-EDC is higher than G-GA but lower than Gn-GA. The ALP gene expression showed drastic down-regulation after day 14 and justified the bone regeneration pattern. Besides, all cryogels had higher relative ALP mRNA expression in OM than NM due to additional induction factors in the medium.

A similar trend followed in COL I expression, where Gn-EDC still dominated over other cryogels and OM resulted in the highest value as seen for ALP. Confirming the early stage marker, the relative mRNA expression of COL I also down-regulated drastically on day 21 and 28 in both culture media to validate the correct osteogenic differentiation
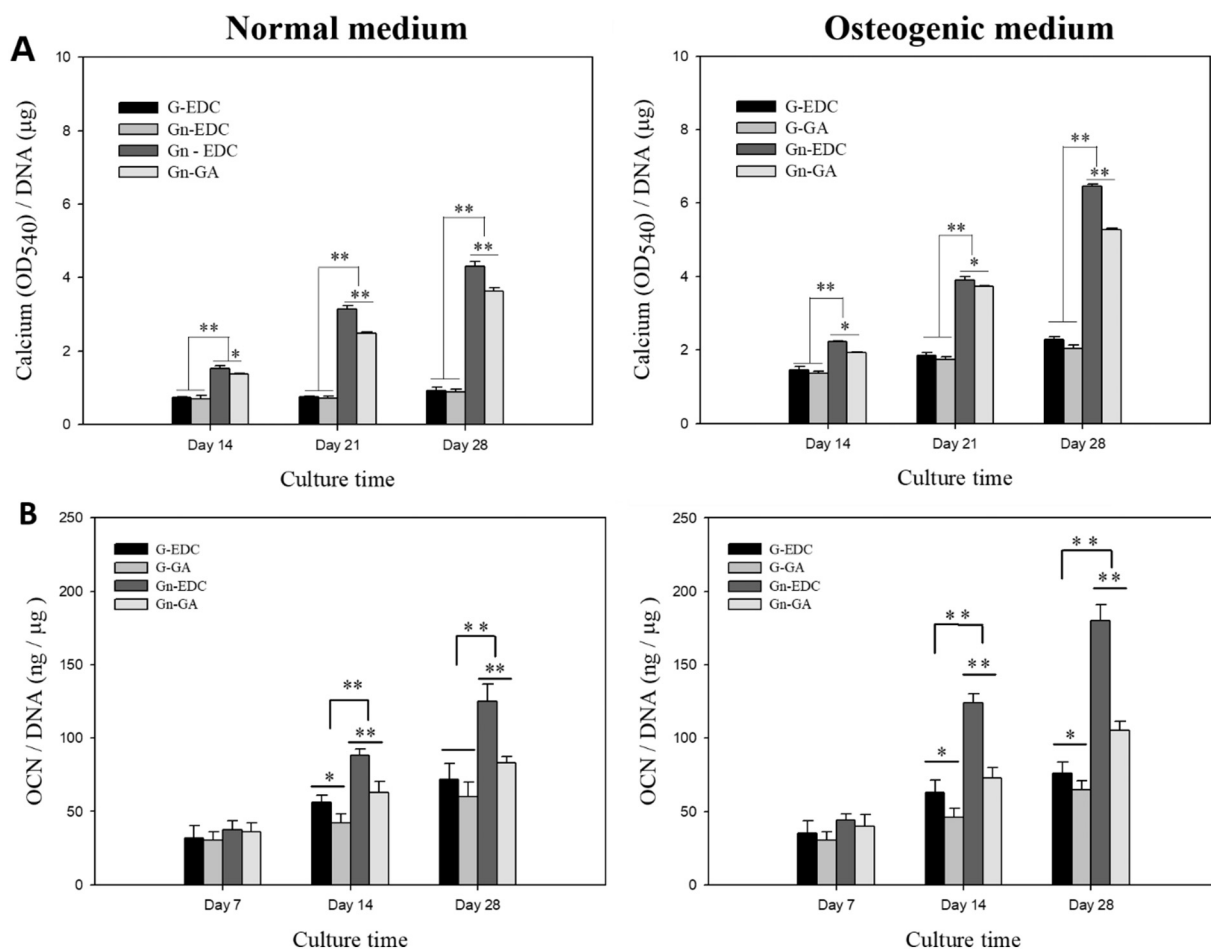
Fig. 9. The normalized calcium (A) and osteopontin (OCN) (B) content of BMSCs when cultured in different cryogels using normal medium and osteogenic medium. $*p < 0.05$, $**p < 0.01$.

pattern. In contrast, OCN and OPN illustrated a different gene expression trend as they belong to the mid-late stage markers. Unlike ALP and COL I, the relative mRNA expression of OCN and OPN were much lower on day 3 and 7 in NM and OM but displayed an exponential increase in later periods to reach the maximum on day 21 or 28. Considering Gn-EDC, the maximum mRNA expression of ALP in OM was 1.67 folds that in NM, while COL I, OCN and OPN were upregulated 1.35, 1.38 and 1.42 folds, respectively, taking 14 days as a reference point for ALP and COL I and 28 days for OCN and OPN. Overall, BMSCs in different cryogel scaffolds followed a pattern of osteogenic gene expression in the order of Gn-EDC > Gn-GA > G-EDC > G-GA, which is consistent with the quantitative results observed for ALP activity and calcium and OCN quantifications. Thus qPCR results thus validated the advantage of using Gn-EDC cryogel for faster differentiation of BMSCs to osteoblasts.

3.3. In vitro dynamic cell culture in a bioreactor

As Gn-EDC provides the best chemical cues for osteogenic differentiation of BMSCs, it was further explored to combine physical cues for osteogenesis through cyclic compression dynamic cell culture (30% and 60% strain) in a bioreactor, by taking advantage of its excellent elastic properties shown in Fig. 5. The effect of mechanical loading of cryogels towards the biological outcome was evaluated based on cell proliferation, ALP activity, mineralization, calcium content, cytoskeletal expression, immunofluorescence staining of COL I and gene expression. In bone tissue engineering, mechanical loading could be an important factor, as it is well known that bone functionally adapts to physical forces. Many reports including in vivo studies confirmed the importance

of mechano-sensitivity in modeling and remodeling processes of bone tissue, in the interaction between biomaterial and bone and in fracture healing [65,66]. Fig. 11A reveals the effect of dynamic culture and the extent of compression strain on cell proliferation. BMSCs cultured at 60% strain in dynamic culture showed the highest proliferation rate while 30% strain in dynamic culture resulted in the least cell growth. The cell proliferation rate could be inversely correlated with cell differentiation as shown in Fig. 11B. The highest ALP activity of 30% compressed Gn-EDC cryogel should be due to the effect of mechanical stimulation in NM without osteogenic factors, which serves as a physical cue for osteogenic differentiation. Interestingly, the ALP activity of the dynamic-60% group was much lower while cell proliferation was much higher than that of the static group. This may indicate an adverse effect of over-strained compression on BMSC differentiation during dynamic cell culture [67]. Indeed, the non-linear stress-strain curve of Gn-EDC cryogel under compression (Fig. 4A) indicated that 60% strain caused a shoot up in stress experienced by the cryogel. This may be one of the reasons that BMSCs react adversely to 60% strain rate and resulted in a lower ALP activity even than the static group. In a study reported by Kyung et al. [68], stimulation triggered by moderate 19.3% mechanical strain resulted in differentiation of pre-osteoblasts.

From SEM observations, BMSCs in dynamically cultured cryogel under 30% strain showed abundant mineral deposition while more spread cells covering up the pores could be observed in dynamically cultured cryogel under 60% strain (Fig. 11C). This is due to the combined effect of nHAP and mechanical stimulation to synergistically trigger BMSC differentiation. The effect of mechanical stimulation may be compared with the osteogenic induction factors in OM from the

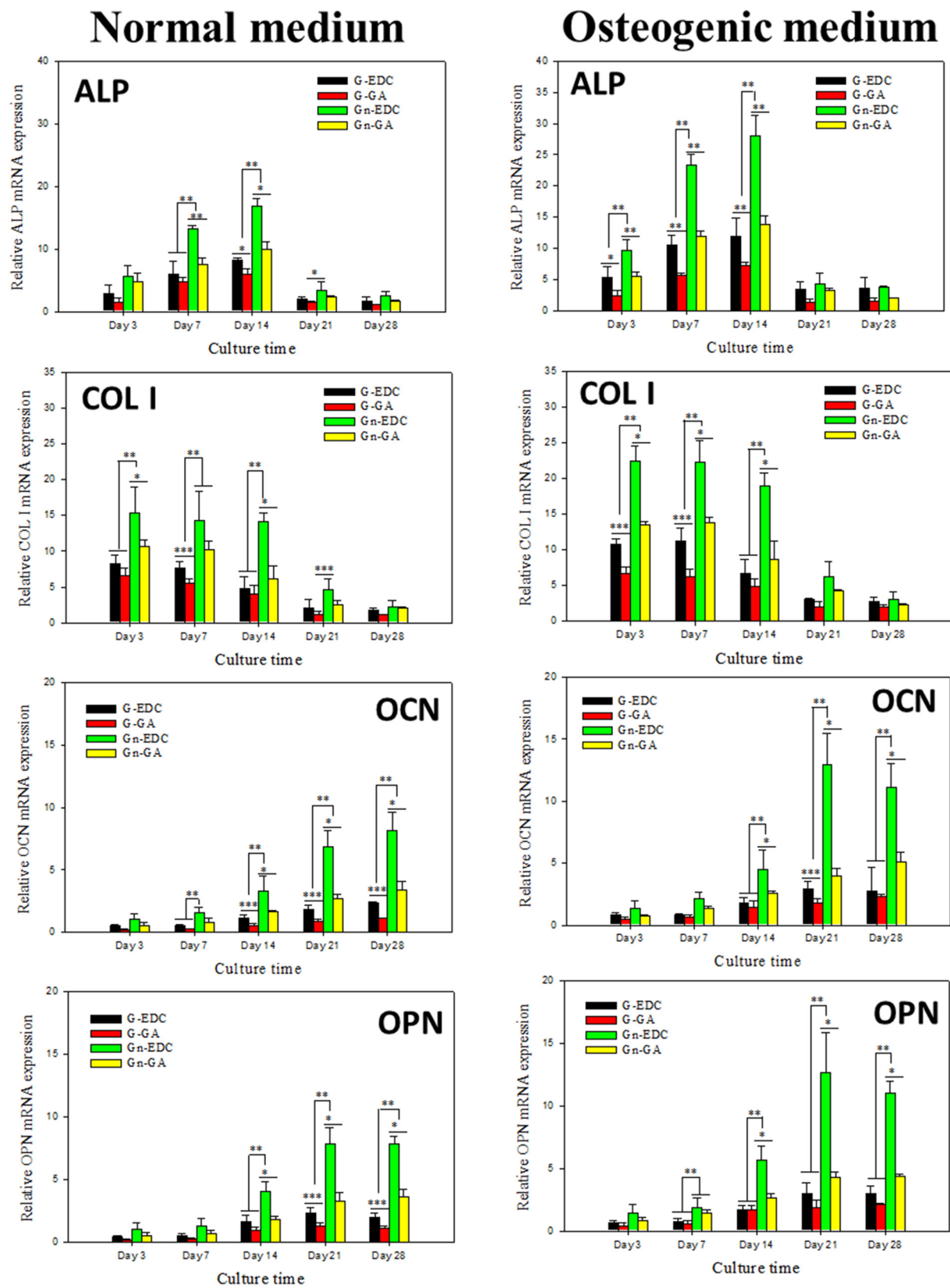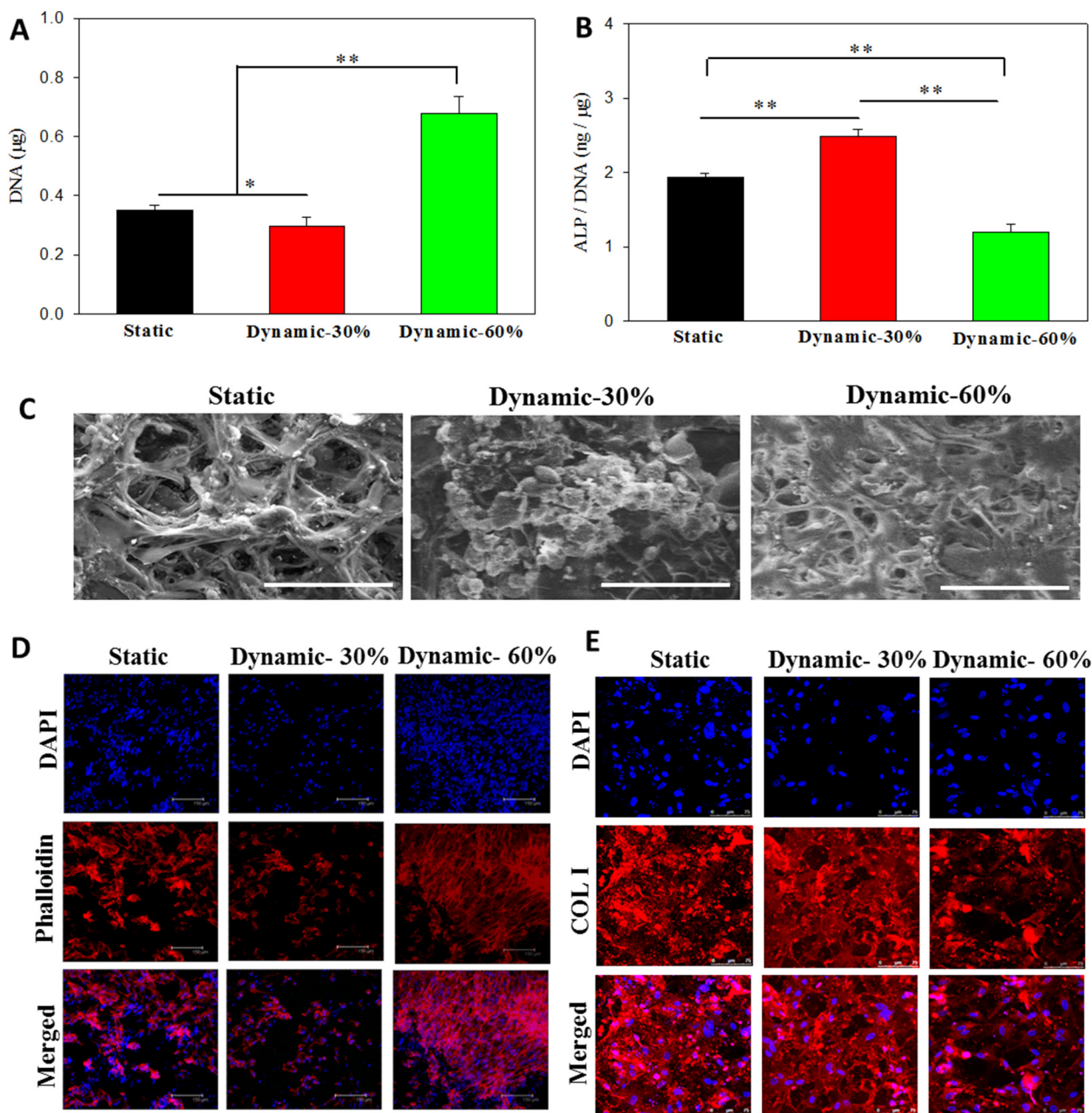**Fig. 10.** The relative alkaline phosphatase (ALP), collagen type I (COL I), osteocalcin (OCN) and osteopontin (OPN) mRNA expression of BMSCs when cultured in different cryogels using normal medium and osteogenic medium. $*p < 0.05$, $**p < 0.01$.

Fig. 11. DNA content (A), normalized alkaline phosphatase (ALP) activity (B), SEM/EDS analysis (C, bar = 100 μm), cytoskeletal actin staining by phalloidin conjugation (D, bar = 150 μm) and immunofluorescence staining of collagen type I (COL I) (E, bar = 75 μm) 14 days after static and dynamic culture (30% or 60% compression strain) of BMSCs in Gn-EDC cryogel in normal medium. *$p < 0.05$, **$p < 0.01$.

mineralization of BMSCs in Gn-EDC in Fig. 8. Nonetheless, higher mineral deposition in the dynamic-30% group confirms that mechanical stimulation could induce BMSCs towards the osteogenic lineage even in the absence of osteogenic induction factors [20]. ALP activity and cell mineralization thus reveal that under mechanical stimulation, NM could replace OM for efficient osteogenesis of BMSCs.

The morphology of BMSCs in Gn-EDC cryogel was further validated through staining of the actin cytoskeleton of adhered cells (Fig. 11D). A well-organized arrangement of the phalloidin-conjugated cytoskeleton was observed in static and dynamic-30% groups with DAPI staining confirming cell nuclei, where the anisotropic spreading of cells endorses normal cell spreading pattern. However, a totally different actin filament organization was observed in the dynamic-60% group with more elongated compressed cell spreading pattern. The higher DAPI-stained nuclear density observed in the dynamic-60% group also correlates

with its high cell proliferation rate from DNA quantification (Fig. 11A). Moreover, the merged images also disclose the spatial homogeneity of cellular distribution within the cryogel scaffolds, which is necessary for 3D cellular growth during tissue formation. The effects of cyclic compression on COL I protein production, which is the major protein component of the bone ECM, were further examined from immunofluorescence staining and confocal microscopy. As shown in Fig. 11E, the COL I secreted by BMSCs was stained red using Cy3-conjugated secondary antibody while the blue color was due to DAPI-stained nuclei. Uniform distribution of COL I was confirmed with the 60%-dynamic group showing relatively the lowest COL I fluorescence intensity. A semi-quantitative evaluation of COL I content was performed using an image analysis software (PAX-it!™) to compare the COL I content. For this purpose, the area percentages of red-stained COL I were normalized with the cell number from DAPI staining in each confocal
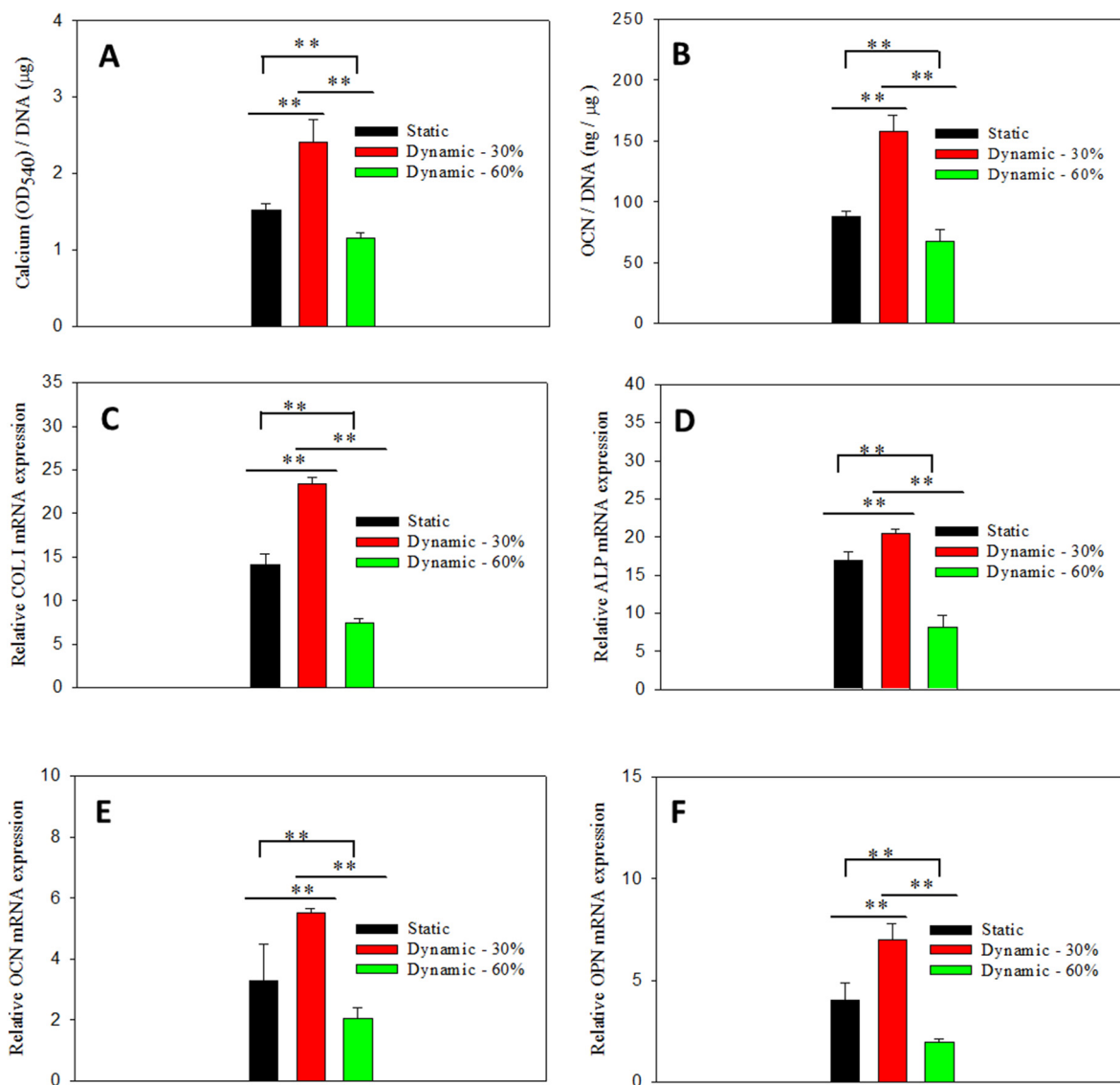
Fig. 12. Normalized calcium content (A), OCN content (B) and relative mRNA expression of COL I (C), ALP (D), OCN (E) and OPN (F) 14 days after static and dynamic culture (30% or 60% compression strain) of BMSCs in Gn-EDC cryogels. **p < 0.01.

image. The normalized COL I contents were 0.88, 1.36 and 0.28 for static, dynamic-30% and dynamic-60%, respectively. Similar to ALP production, static culture resulted in 3.1-fold specific COL I production over dynamic-60%, while dynamic-30% resulted in 4.9-fold specific COL I production over dynamic-60%. All results cross-confirm that dynamic culture with 30% strain offered the best culture condition for BMSC differentiation towards osteoblasts.

From Fig. 12A, the calcium content through static culture was compared with both dynamic cultured cryogels and the values after normalized to DNA content were reported in terms of optical density (OD_{540}). Similar to previous results, 30% dynamic culture resulted in the highest calcium deposition while 60% the lowest. Specifically, the OD_{540}/DNA value of the dynamic-30% group was 1.57 and 2.09 folds that of the static and dynamic-60% groups, confirming the advantage of a lower compression ratio towards cell differentiation. It is interesting to note that the mean normalized calcium content (OD_{540}/µg) of Gn-EDC in OM with static culture was ~2.1 on day 14 (Fig. 9A). In comparison, dynamic culture in NM at 30% compression ratio was ~2.4 at the same time point. All findings extrapolating the dominance of low level dynamic compression of cryogels towards faster mineral deposition was further re-verified through OCN quantification (Fig. 12B).

Indeed, the trend of normalized OCN value was similar to that shown for calcium quantification in the order of dynamic-30% > static > dynamic-60%. All results are consistent with the lower cell proliferation rate and higher ALP production (Fig. 11A, B), higher mineral deposition from SEM/EDS images (Fig. 11C) as well as higher COL I production (Fig. 11E) observed earlier.

By assessing the expression of relevant osteogenic marker genes through q-PCR, the specific mRNA expression levels of COL I (Fig. 12C), ALP (Fig. 12D), OCN (Fig. 12E) and OPN (Fig. 12F) followed the same trend as observed for ALP activity, calcium deposition and OCN quantification with dynamic-30% > static > dynamic-60%. Being early and mid-stage differentiation genes, COL I and ALP had the highest expression values of 20.5 and 23.4, in comparison to 5.5 and 7.0 for the late expressing OCN and OPN in the dynamic-30% group on day 14. Those values could be compared with the relative mRNA expression levels of BMSCs in Gn-EDC under static culture in OM, which were 19.0, 28.0, 4.5 and 5.7 for COL I, ALP, OCN and OPN, respectively (Fig. 10). The similar gene expression patterns thus points out the fact that dynamic culture at 30% compression could induce osteogenic differentiation of BMSCs to the same extent as that induced by osteogenic factors in OM during static culture. Taken together, we concluded
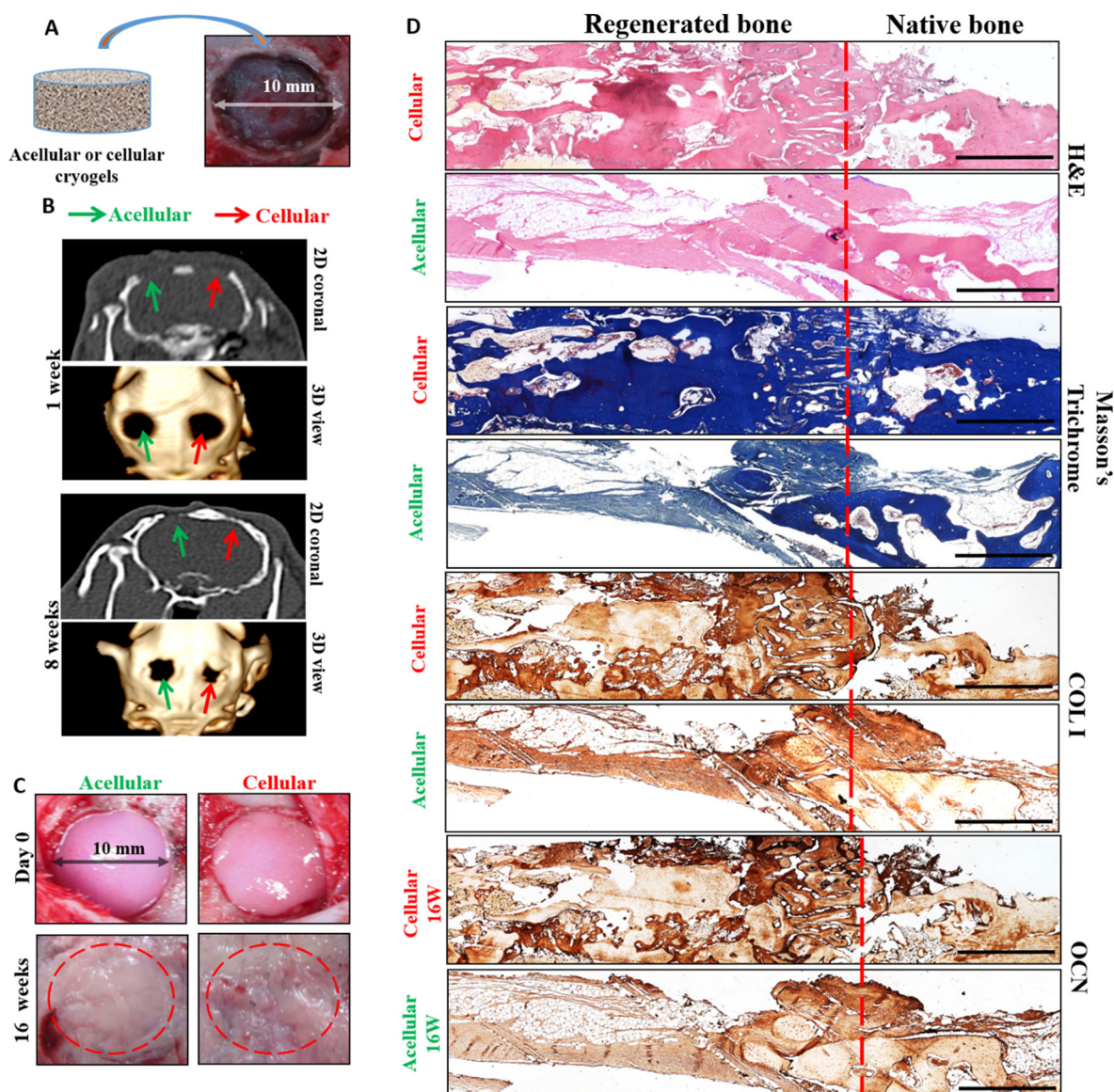
Fig. 13. (A) The schematic of acellular or cellular cryogel implantation in 10-mm rabbit cranial bone defect. (B) 2D coronal and 3D computed tomography (CT) images 1 and 8 weeks post-implantation of acellular or cellular cryogels. The green arrow denotes the defect site implanted with an acellular cryogel while the red arrow represents the site implanted with a cellular cryogel. (C) Gross views of cranial bone defect sites immediately after surgery and 16 weeks post-implantation. (D) Histological (H&E, Masson's trichrome) staining and immunohistochemical staining of COL I and OCN of the cellular and acellular samples 16 weeks post-implantation (bar = 500 μm). (For interpretation of the references to color in this figure legend, the reader is referred to the web version of this article.)

that dynamic culture of BMSCs in Gn-EDC cryogels in a bioreactor with 30% compression strain provides effective physical cues for osteogenic differentiation of BMSCs.

3.4. In vivo animal studies

As *in vitro* dynamic cell culture experiments revealed the significance of mechanical stimulation in a bioreactor for osteogenic differentiation of BMSCs in Gn-EDC cryogels using NM, *in vivo* animal experiments followed to confirm the bone formation ability of *in vitro* cultured scaffold/cell constructs. Fig. 13A is the schematic of implantation of acellular or cellular cryogels in rabbit calvarial 10-mm critical size defects. The Gn-EDC/BMSCs constructs dynamically cultured at 30% strain in NM for 14 days were implanted in the right cranial bone defects (cellular) while blank Gn-EDC cryogels (acellular) were implanted in the left cranial bone defects for comparison.

All animals were allowed to undergo CT evaluation 1 and 8 weeks post-operation (Fig. 13B), where the top panel at each time point

displays the 2D coronal view while the bottom panel shows the 3D reconstructed image. The green arrow denotes the defect site implanted with an acellular cryogel while the red arrow represents the site implanted with a cellular cryogel in the CT images. No distinguishable difference between each defect site was observed from the CT images after 1 week as the broken white line in the 2D coronal view and the empty hole in the 3D CT image indicated no new bone formation at the defect sites for both groups. The CT image density of the acellular group scarcely increased after 8 weeks. In contrast, the image density of the cellular group elevated significantly and the broken white line from the 2D image or the empty hole from the 3D image was partially filled, indicating new bone formation. New bone tissue bridging the defect site to the surrounding bone was only observed for the cellular group in the 2D coronal view with the defect diameter shrinking to a much smaller size in the 3D view (Fig. 13B).

After anesthetization, all animals were euthanized for gross view observation and specimen were removed for histology 16 weeks post-implantation (Fig. 13C). From gross view, both implanted sites

appeared to be normal without swelling or necrosis while clinical complications like infection, wound breakdown or exudate were not observed. The acellular site appeared to be softer and whitish compared to the uniform hard nature of the cellular site (circled within red dotted lines). Slight red spots found within the cellular sample may be due to new blood vessel formation, which is beneficial for bone regeneration.

Histological evaluation of new bone formation and tissue development was further confirmed through H&E and Masson's trichrome staining and IHC staining of COL I and OCN (Fig. 13D). An average of eight images were recorded for each stained image and stitched together using a commercial software to show the repaired site and its surroundings to include both native bone and regenerated bone for comparison. The H&E staining showed drastic difference in cell number in the form of osteoblasts between cellular and acellular groups. For the cellular group, a uniform cellular distribution was observed throughout the regenerated area and the ECM was oriented in a native fashion indicating growth of bone tissue in the defect region. However, the acellular group had neither cell proliferation nor ECM deposition within the center, with cells found only in the marginal area due to cell migration from peripheral native bone.

Bone regeneration was further verified through Masson's trichrome staining. Osteoid, the un-mineralized organic portion of the bone matrix, will be secreted by osteoblasts during differentiation of BMSCs and embedded in the newly formed bone tissue matrix. Since mineralized osteoid will combine with adjacent bone cells and develop into new bone tissue, a blue staining through Masson's trichrome provides a good indication of new bone formation. As shown in Fig. 13D, the cellular group had deep blue-colored stains throughout the section and had no difference in intensity from surrounding native bone, which accounts for osteoid formation and bone regeneration. The acellular group revealed significantly lower level of staining intensity and the light blue color observed in the defect region close to the native bone should be due to post-operative osteoblast migration from the native tissue and thus accounts for the presence of few nuclei as observed from H&E stain. Although the color intensity in the native bone area of the acellular group was similar to that of the cellular group, the dominant white empty area in the defect region of the acellular group clearly implies the lack of regeneration in the absence of BMSCs. Indeed, the empty white region in the acellular group symbolizes the lack of regeneration while the dark blue color in the cellular group defines the presence of mature bone with the formation of new osteoid bodies.

It should be pointed out that although successful repair of rabbit critical-sized cranial bone defect was demonstrated using mechanically stimulated BMSCs in Gn-EDC cryogels, the bone regeneration effect may not be very high. We ascribe this limitation to the time of observation, which was only 8 weeks post-implantation. Besides, no osteogenic growth factor was incorporated in the scaffolds while the cell/scaffold construct was cultured *in vitro* dynamically in NM for 14 days before implantation. Despite the excellent biocompatibility and osteoconductivity of nHAP, Gn-EDC cryogels may not have high osteoinductivity for bone tissue engineering application [69]. Incorporation of osteoinductive materials in the composite cryogel should be an appealing strategy to enhance the osteogenic differentiation of seeded BMSCs [70]. We believe that higher bone regeneration ability could be accomplished by employing a longer implantation time (*e.g.* 16 weeks) or by introducing bone morphogenetic protein 2 (BMP-2) to the composite cryogel scaffolds as demonstrated from our previous study [22].

Other than confirmation of cellular distribution of differentiated BMSCs and the presence of newly formed bone tissue by H&E and Masson's trichrome staining, the presence of bone marker proteins in the ECM was confirmed by IHC staining of COL I and OCN (Fig. 13D). Positive staining of COL I and OCN could confirm bone regeneration through mid-later stage osteogenic differentiation. The brown color intensity in the tissue section of the cellular sample was much higher compared to the acellular sample, both for COL I and OCN. The uniform distribution of intense brown color throughout the cellular sample confirms that BMSCs proliferated in a 3D fashion throughout the cryogel scaffold and differentiated into osteoblasts. The uniform cellular distribution and cell differentiation should have been achieved through the interconnected macro-porous structure of BMSC-seeded cryogels while the low intensity brown color with empty white background observed for the acellular cryogel proves the lack of bone formation in the absence of BMSCs. In short, both histology and IHC staining conclude the superior bone regeneration efficacy of mechanically stimulated BMSC-seeded Gn-EDC cryogels for effective bone replacement or repair.

4. Conclusions

Cryogel scaffolds for bone tissue engineering applications could be prepared from 5% gelatin solution with or without replacing half gelatin with nHAP, using two different cross-linking agents (EDC and GA). SEM analysis confirmed the macroporous morphology with interconnected pores for all cryogels while FTIR, XRD and EDS revealed the presence of nHAP in composite cryogels. nHAP incorporation did not significantly influence the structure of the cryogels with ~80% porosity to be ideal for bone regeneration. G cryogels had significantly higher swelling ratios in water than Gn. Incorporation of nHAP in cryogels leads to faster *in vitro* degradation rates concomitant with lower degrees of crosslinking. Cryogels crosslinked with GA displayed higher degradation resistance and lesser swelling in water due to denser polymer network formation, which was also revealed from their better mechanical properties. Static *in vitro* culture confirmed the dominance of Gn-EDC cryogel cultured in OM towards BMSC differentiation. Gn-EDC seeded with BMSCs and cultured dynamically in a bioreactor with a moderate (30%) strain was the best culture condition for faster bone regeneration *in vitro*. This *in vitro* cultured cell/scaffold construct was useful for repair of rabbit cranial bone defect *in vivo* from CT and histology analysis. In short, our results first revealed change in physical properties due to nHAP-incorporation and the use of different cross-linking agents (EDC and GA), followed by revealing the dominance of EDC over GA on BMSC osteogenic differentiation. It further demonstrated enhanced osteogenesis efficacy of BMSCs in Gn-EDC cryogels through dynamic culture with a properly chosen mechanical stimulation condition in a bioreactor. Finally, such *in vitro*-cultured constructs could be useful for bone repair in an animal model. Therefore, by exploring chemical and physical cues offered by cryogels for bone regeneration using BMSCs *in vitro* and *in vivo*, this study could be taken as an ideal reference in process development of advanced biomaterials for bone tissue engineering.

Acknowledgements

References

[1] J.L. Drury, D.J. Mooney, Hydrogels for tissue engineering: scaffold design variables and applications, Biomaterials 24 (2003) 4337–4351.

[2] M.P. Lutolf, J.A. Hubbell, Synthetic biomaterials as instructive extracellular microenvironments for morphogenesis in tissue engineering, Nat. Biotechnol. 23 (2005) 47–55.

[3] G. Iviglia, C. Cassinelli, D. Bollati, F. Baino, E. Torre, M. Morra, C. Vitale-Brovarone, Engineered porous scaffolds for periprosthetic infection prevention, Mater. Sci. Eng. C 68 (2016) 701–715.

[4] K.Y. Lee, D.J. Mooney, Hydrogels for tissue engineering, Chem. Rev. 101 (2001) 1869–1880.

[5] B. Balakrishnan, N. Joshi, A. Jayakrishnan, R. Banerjee, Self-crosslinked oxidized alginate/gelatin hydrogel as injectable, adhesive biomimetic scaffolds for cartilage

regeneration, Acta Biomater. 10 (2014) 3650–3663.

[6] S.A. Poursamar, J. Hatami, A.N. Lehner, C.L. da Silva, F.C. Ferreira, A.P.M. Antunes, Potential application of gelatin scaffolds prepared through in situ gas foaming in skin tissue engineering, Int. J. Polym. Mater. Polym. Biomater. 65 (2016) 315–322.

[7] X. Liu, L.A. Smith, J. Hu, P.X. Ma, Biomimetic nanofibrous gelatin/apatite composite scaffolds for bone tissue engineering, Biomaterials 30 (2009) 2252–2258.

[8] D.B. Burr, O. Akkus, Bone morphology and organization, in: D.B. Burr, M.R. Allen (Eds.), Basic and Applied Bone Biology, Academic Press, San Diego, 2014, pp. 3–25.

[9] H.-W. Kim, J.-H. Song, H.-E. Kim, Nanofiber generation of gelatin–hydroxyapatite biomimetics for guided tissue regeneration, Adv. Func. Mater. 15 (2005) 1988–1994.

[10] H. Kim, L. Che, Y. Ha, W. Ryu, Mechanically-reinforced electrospun composite silk fibroin nanofibers containing hydroxyapatite nanoparticles, Mater. Sci. Eng. C 40 (2014) 324–335.

[11] J. Venkatesan, S.K. Kim, Nano-hydroxyapatite composite biomaterials for bone tissue engineering - a review, J. Biomed. Nanotechnol. 10 (2014) 3124–3140.

[12] H. Zhou, J. Lee, Nanoscale hydroxyapatite particles for bone tissue engineering, Acta Biomater. 7 (2011) 2769–2781.

[13] E. Pepla, L.K. Besharat, G. Palaia, G. Tenore, G. Migliau, Nano-hydroxyapatite and its applications in preventive, restorative and regenerative dentistry: a review of literature, Ann. Stomatol. 5 (2014) 108–114.

[14] L. Meirelles, A. Arvidsson, M. Andersson, P. Kjellin, T. Albrektsson, A. Wennerberg, Nano hydroxyapatite structures influence early bone formation, J. Biomed. Mater. Res. Part A 87 (2008) 299–307.

[15] J. Ji, X. Tong, X. Huang, T. Wang, Z. Lin, Y. Cao, J. Zhang, L. Dong, H. Qin, Q. Hu, Sphere-shaped nano-hydroxyapatite/chitosan/gelatin 3D porous scaffolds increase proliferation and osteogenic differentiation of human induced pluripotent stem cells from gingival fibroblasts, Biomed. Mater. 10 (2015) 045005.

[16] S.A. Bencherif, T.M. Braschler, P. Renaud, Advances in the design of macroporous polymer scaffolds for potential applications in dentistry, J. Periodontal Implant Sci. 43 (2013) 251–261.

[17] Y. Privar, I. Malakhova, A. Pestov, A. Fedorets, Y. Azarova, S. Schwarz, S. Bratskaya, Polyethyleneimine cryogels for metal ions sorption, Chem. Eng. J. 334 (2018) 1392–1398.

[18] K.H. Chang, H.T. Liao, J.P. Chen, Preparation and characterization of gelatin/ hyaluronic acid cryogels for adipose tissue engineering: in vitro and in vivo studies, Acta Biomater. 9 (2013) 9012–9026.

[19] A. Sharma, S. Bhat, V. Nayak, A. Kumar, Efficacy of supermacroporous poly(ethylene glycol)-gelatin cryogel matrix for soft tissue engineering applications, Mater. Sci. Eng. C 47 (2015) 298–312.

[20] J.R. Mauney, S. Sjostorm, J. Blumberg, R. Horan, J.P. O'Leary, G. Vunjak-Novakovic, V. Volloch, D.L. Kaplan, Mechanical stimulation promotes osteogenic differentiation of human bone marrow stromal cells on 3-D partially demineralized bone scaffolds in vitro, Calcified Tissue Int. 74 (2004) 458–468.

[21] E.Y. Chao, N. Inoue, Biophysical stimulation of bone fracture repair, regeneration and remodelling, Eur. Cells & Mater. 6 (2003) 72–84.

[22] H.-T. Liao, K.T. Shalumon, K.-H. Chang, C. Sheu, J.-P. Chen, Investigation of synergistic effects of inductive and conductive factors in gelatin-based cryogels for bone tissue engineering, J. Mater. Chem. B 4 (2016) 1827–1841.

[23] E. Saino, L. Fassina, S. Van Vlierberghe, M.A. Avanzini, P. Dubruel, G. Magenes, L. Visai, F. Benazzo, Effects of electromagnetic stimulation on osteogenic differentiation of human mesenchymal stromal cells seeded onto gelatin cryogel, Int. J. Immunopathology & Pharma 24 (2011) 1–6.

[24] L. Fassina, E. Saino, L. Visai, J. Schelfhout, M. Dierick, L. Van Hoorebeke, P. Dubruel, F. Benazzo, G. Magenes, S. Van Vlierberghe, Electromagnetic stimulation to optimize the bone regeneration capacity of gelatin-based cryogels, Int. J. Immunopathology & Pharma 25 (2012) 165–174.

[25] L. Fassina, L. Visai, G. Magenes, J. Schelfhout, N. Bloise, F. Riva, C. Omes, M.A. Avanzini, M.G.C.D. Angelis, F. Benazzo, M. Dierick, L.V. Hoorebeke, P. Dubruel, S.V. Vlierberghe, Ultrasound stimulus to enhance the bone regeneration capability of gelatin cryogels, 2013 35th Annual International Conference of the IEEE Engineering in Medicine and Biology Society, 2013, pp. 846–849.

[26] R. Mishra, D.B. Raina, M. Pelkonen, L. Lidgren, M. Tagil, A. Kumar, Study of in vitro and in vivo bone formation in composite cryogels and the influence of electrical stimulation, Int. J. Biol. Sci. 11 (2015) 1325–1336.

[27] Y. Yang, J.L. Magnay, L. Cooling, H.A. El, Development of a 'mechano-active' scaffold for tissue engineering, Biomaterials 23 (2002) 2119–2126.

[28] T. Davisson, S. Kunig, A. Chen, R. Sah, A. Ratcliffe, Static and dynamic compression modulate matrix metabolism in tissue engineered cartilage, J. Orthop. Res. 20 (2002) 842–848.

[29] B.S. Kim, D.J. Mooney, Scaffolds for engineering smooth muscle under cyclic mechanical strain conditions, J. Biomech. Eng. 122 (2000) 210–215.

[30] W.H. Zimmermann, K. Schneiderbanger, P. Schubert, M. Didie, F. Munzel, J.F. Heubach, S. Kostin, W.L. Neuhuber, T. Eschenhagen, Tissue engineering of a differentiated cardiac muscle construct, Circulation Res 90 (2002) 223–230.

[31] W.-J. Shih, Y.-F. Chen, M.-C. Wang, M.-H. Hon, Crystal growth and morphology of the nano-sized hydroxyapatite powders synthesized from CaHPO$_4$·2H$_2$O and CaCO$_3$ by hydrolysis method, J. Crystal Growth 270 (2004) 211–218.

[32] K.S. Rho, L. Jeong, G. Lee, B.-M. Seo, Y.J. Park, S.-D. Hong, S. Roh, J.J. Cho, W.H. Park, B.-M. Min, Electrospinning of collagen nanofibers: effects on the behavior of normal human keratinocytes and early-stage wound healing, Biomaterials 27 (2006) 1452–1461.

[33] A. Jena, K. Gupta, Characterization of pore structure of filter media, Fluid - Particle Sep. J. 14 (2002) 227–241.

[34] A.F.S.A. Habeeb, Determination of free amino groups in proteins by trinitrobenzenesulfonic acid, Anal. Biochem. 14 (1966) 328–336.

[35] S.L.Y. Woo, M.A. Gomez, W.H. Akeson, The time and history-dependent viscoelastic properties of the canine medial collateral ligament, J. Biomech. Eng. 103 (1981) 293–298.

[36] C.H. Chen, C.Y. Kuo, J.P. Chen, Effect of cyclic dynamic compressive loading on chondrocytes and adipose-derived stem cells co-cultured in highly elastic cryogel scaffolds, Int. J. Mol. Sci. 19 (2018) 370.

[37] Y.-J. Kim, R.L.Y. Sah, J.-Y.H. Doong, A.J. Grodzinsky, Fluorometric assay of DNA in cartilage explants using Hoechst 33258, Anal. Biochem. 174 (1988) 168–176.

[38] G.J. Lai, K.T. Shalumon, S.H. Chen, J.P. Chen, Composite chitosan/silk fibroin nanofibers for modulation of osteogenic differentiation and proliferation of human mesenchymal stem cells, Carbohyd. Polym. 111 (2014) 288–297.

[39] G.M. Cunniffe, C.M. Curtin, E.M. Thompson, G.R. Dickson, F.J. O'Brien, Content-dependent osteogenic response of nanohydroxyapatite: an in vitro and in vivo assessment within collagen-based scaffolds, Int. J. Mol. Sci. 8 (2016) 23477–23488.

[40] Y.J. Hwang, J. Granelli, J. Lyubovitsky, Effects of zero-length and non-zero-length cross-linking reagents on the optical spectral properties and structures of collagen hydrogels, Int. J. Mol. Sci. 4 (2012) 261–267.

[41] C.P. Barnes, C.W. Pemble, D.D. Brand, D.G. Simpson, G.L. Bowlin, Cross-linking electrospun type II collagen tissue engineering scaffolds with carbodiimide in ethanol, Tissue Eng. 13 (2007) 1593–1605.

[42] J.E. Eastoe, The amino acid composition of mammalian collagen and gelatin, Biochem. J. 61 (1955) 589–600.

[43] S.N. Park, H.J. Lee, K.H. Lee, H. Suh, Biological characterization of EDC-crosslinked collagen-hyaluronic acid matrix in dermal tissue restoration, Biomaterials 24 (2003) 1631–1641.

[44] G.P. Huang, S. Shanmugasundaram, P. Masih, D. Pandya, S. Amara, G. Collins, T.L. Arinzeh, An investigation of common crosslinking agents on the stability of electrospun collagen scaffolds, J. Biom. Mater. Res. Part A 103 (2015) 762–771.

[45] J. Sundaram, T.D. Durance, R. Wang, Porous scaffold of gelatin–starch with nanohydroxyapatite composite processed via novel microwave vacuum drying, Acta Biomater. 4 (2008) 932–942.

[46] M. Peter, N. Ganesh, N. Selvamurugan, S.V. Nair, T. Furuike, H. Tamura, R. Jayakumar, Preparation and characterization of chitosan–gelatin/nanohydroxyapatite composite scaffolds for tissue engineering applications, Carbohydr. Polym. 80 (2010) 687–694.

[47] I. Inci, H. Kirsebom, I.Y. Galaev, B. Mattiasson, E. Piskin, Gelatin cryogels crosslinked with oxidized dextran and containing freshly formed hydroxyapatite as potential bone tissue-engineering scaffolds, J. Tissue Eng. Regen. Med. 7 (2013) 584–588.

[48] S.J. Hollister, W.L. Murphy, Scaffold translation: barriers between concept and clinic, Tissue Engineering Part B 17 (2011) 459–474.

[49] G. Turnbull, J. Clarke, F. Picard, P. Riches, L. Jia, F. Han, B. Li, W. Shu, 3D bioactive composite scaffolds for bone tissue engineering, Bioact. Mater. 3 (2018) 278–314.

[50] A.K. Shakya, U. Kandalam, Three-dimensional macroporous materials for tissue engineering of craniofacial bone, Brit. J. Oral. Max. Sur. 55 (2017) 875–891.

[51] K.R. Hixon, T. Lu, S.A. Sell, A comprehensive review of cryogels and their roles in tissue engineering applications, Acta Biomater. 62 (2017) 29–41.

[52] M.M. Villa, L. Wang, J. Huang, D.W. Rowe, M. Wei, Bone tissue engineering with a collagen-hydroxyapatite scaffold and culture expanded bone marrow stromal cells, J. Biomed. Mater. Res. Part B 103 (2015) 243–253.

[53] C.H. Chen, C.Y. Kuo, Y.J. Wang, J.P. Chen, Dual function of glucosamine in gelatin/ hyaluronic acid cryogel to modulate scaffold mechanical properties and to maintain chondrogenic phenotype for cartilage tissue engineering, Int. J. Mol. Sci. 17 (2016) 1959.

[54] P. Abdel-Sayed, S.E. Darwiche, U. Kettenberger, D.P. Pioletti, The role of energy dissipation of polymeric scaffolds in the mechanobiological modulation of chondrogenic expression, Biomaterials 35 (2014) 1890–1897.

[55] E. Tsiridis, A. Bhalla, Z. Ali, N. Gurav, M. Heliotis, S. Deb, L. DiSilvio, Enhancing the osteoinductive properties of hydroxyapatite by the addition of human mesenchymal stem cells, and recombinant human osteogenic protein-1 (BMP-7) in vitro, Injury 37 (Suppl. 3) (2006) S25–S32.

[56] I. Nishimura, R. Hisanaga, T. Sato, T. Arano, S. Nomoto, Y. Ikada, M. Yoshinari, Effect of osteogenic differentiation medium on proliferation and differentiation of human mesenchymal stem cells in three-dimensional culture with radial flow bioreactor, Regen. Ther. 2 (2015) 24–31.

[57] G.M. Boland, G. Perkins, D.J. Hall, R.S. Tuan, Wnt 3a promotes proliferation and suppresses osteogenic differentiation of adult human mesenchymal stem cells, J. Cell. Biochem. 93 (2004) 1210–1230.

[58] R.S. Siffert, The role of alkaline phosphatase in osteogenesis, J. Exp. Med. 93 (1951) 415–426.

[59] B.H. C., L.Q. C., L. Yanan, L. Hang, B.-S. Donna, L. Li, T.R. S., R.L. J., S.P. H., N.D. J., Osteoblast differentiation and bone matrix formation in vivo and in vitro, Tissue Eng. Part B: Reviews 23 (2017) 268–280.

[60] G. Toskas, C. Cherif, R.D. Hund, E. Laourine, B. Mahltig, A. Fahmi, C. Heinemann, T. Hanke, Chitosan(PEO)/silica hybrid nanofibers as a potential biomaterial for bone regeneration, Carbohydr. Polym. 94 (2013) 713–722.

[61] M. Ngiam, S. Liao, A.J. Patil, Z. Cheng, C.K. Chan, S. Ramakrishna, The fabrication of nano-hydroxyapatite on PLGA and PLGA/collagen nanofibrous composite scaffolds and their effects in osteoblastic behavior for bone tissue engineering, Bone 45 (2009) 4–16.

[62] S. Cremers, P. Garnero, M.J. Seibel, Biochemical markers of bone metabolism, in: J.P. Bilezikian, L.G. Raisz, T.J. Martin (Eds.), Principles of Bone Biology, Third edition, Academic Press, San Diego, 2008, pp. 1857–1881.

[63] Y. Wang, Y. Wei, X. Zhang, M. Xu, F. Liu, Q. Ma, Q. Cai, X. Deng, PLGA/PDLLA core–shell submicron spheres sequential release system: preparation, characterization and promotion of bone regeneration in vitro and in vivo, Chem. Eng. J. 273

(2015) 490–501.

[64] A. Hughes, Analysis of gene expression in bone by quantitative RT/PCR, Methods Mol. Biol. 816 (2012) 261–275.

[65] A.E. Goodship, J.L. Cunningham, J. Kenwright, Strain rate and timing of stimulation in mechanical modulation of fracture healing, Clin. Orthop. Relat. Res. (1998) S105–S115.

[66] V.I. Sikavitsas, J.S. Temenoff, A.G. Mikos, Biomaterials and bone mechanotransduction, Biomaterials 22 (2001) 2581–2593.

[67] G. Bouet, D. Marchat, M. Cruel, L. Malaval, L. Vico, In vitro three-dimensional bone tissue models: from cells to controlled and dynamic environment, Tissue Eng. Part B 21 (2015) 133–156.

[68] K.S. Kang, S.-J. Lee, H. Lee, W. Moon, D.-W. Cho, Effects of combined mechanical stimulation on the proliferation and differentiation of pre-osteoblasts, Exp. Mol. Med. 43 (2011) 367.

[69] P. Habibovic, K. de Groot, Osteoinductive biomaterials–properties and relevance in bone repair, J. Tissue Eng. Regen. Med. 1 (2007) 25–32.

[70] G.E. Friedlaender, S. Lin, L.A. Solchaga, L.B. Snel, S.E. Lynch, The role of recombinant human platelet-derived growth factor-BB (rhPDGF-BB) in orthopaedic bone repair and regeneration, Curr. Pharm. Des. 19 (2013) 3384–3390.